



RNA knockdown by synthetic peptidyl-oligonucleotide ribonucleases: behavior of recognition and cleavage elements under physiological conditions

Mengisteab Gebrezgiabher, Waleed A. Zalloum, David J. Clarke, Steven M. Miles, Antonina A. Fedorova, Marina A. Zenkova & Elena V. Bichenkova

To cite this article: Mengisteab Gebrezgiabher, Waleed A. Zalloum, David J. Clarke, Steven M. Miles, Antonina A. Fedorova, Marina A. Zenkova & Elena V. Bichenkova (2020): RNA knockdown by synthetic peptidyl-oligonucleotide ribonucleases: behavior of recognition and cleavage elements under physiological conditions, Journal of Biomolecular Structure and Dynamics, DOI: [10.1080/07391102.2020.1751711](https://doi.org/10.1080/07391102.2020.1751711)

To link to this article: <https://doi.org/10.1080/07391102.2020.1751711>



© 2020 The Author(s). Published by Informa UK Limited, trading as Taylor & Francis Group



[View supplementary material](#)



Published online: 16 Apr 2020.



[Submit your article to this journal](#)



Article views: 379



[View related articles](#)




[View Crossmark data](#)



Citing articles: 2 [View citing articles](#)

RNA knockdown by synthetic peptidyl-oligonucleotide ribonucleases: behavior of recognition and cleavage elements under physiological conditions

Mengisteab Gebrezgiabher^a, Waleed A. Zalloum^a, David J. Clarke^a, Steven M. Miles^a, Antonina A. Fedorova^b, Marina A. Zenkova^b and Elena V. Bichenkova^a 

^aDivision of Pharmacy and Optometry, School of Health Sciences, Faculty of Biology, Medicine and Health, University of Manchester, Manchester, United Kingdom; ^bInstitute of Chemical Biology and Fundamental Medicine, Siberian Branch of the Russian Academy of Sciences, Novosibirsk, Russia

Communicated by Ramaswamy H. Sarma

ABSTRACT

Sequence-specific *protein-based* ribonucleases are not found in nature. Absolute sequence selectivity in RNA cleavage *in vivo* normally requires multi-component complexes that recruit a guide RNA or DNA for target recognition and a protein–RNA assembly for catalytic functioning (e.g. RNAi molecular machinery, RNase H). Recently discovered peptidyl-oligonucleotide synthetic ribonucleases selectively knock down pathogenic RNAs by irreversible cleavage to offer unprecedented opportunities for control of disease-relevant RNA. Understanding how to increase their potency, selectivity and catalytic turnover will open the translational pathway to successful therapeutics. Yet, very little is known about how these chemical ribonucleases bind, cleave and leave their target. Rational design awaits this understanding in order to control therapy, particularly how to overcome the trade-off between sequence specificity and potency through catalytic turnover. We illuminate this here by characterizing the interactions of these chemical RNases with both complementary and non-complementary RNAs using T_m profiles, fluorescence, UV-visible and NMR spectroscopies. Crucially, the level of counter cations, which are tightly-controlled within cellular compartments, also controlled these interactions. The oligonucleotide component dominated interaction between conjugates and *complementary* targets in the presence of physiological levels of counter cations (K^+), sufficient to prevent repulsion between the complementary nucleic acid strands to allow Watson-Crick hydrogen bonding. In contrast, the positively-charged catalytic peptide interacted poorly with target RNA, when counter cations similarly screened the negatively-charged sugar-phosphate RNA backbones. The peptide only became the key player, when counter cations were insufficient for charge screening; moreover, only under such non-physiological conditions did conjugates form strong complexes with *non-complementary* RNAs.

ARTICLE HISTORY

Received 18 December 2019
Accepted 27 March 2020

KEYWORDS

RNA; cleavage; chemical ribonucleases; conjugate; fluorescence; hybridization; self-assembly


1. Introduction

Bioconjugates with controlled chemical properties can be designed with new biological functionality as a basis for therapeutic innovation to provide solutions to complex biological challenges, which are currently unmet by conventional drug discovery approaches (Scannell et al., 2012). One of the major health care priorities is to develop highly-selective treatments against abnormal gene expression in disease states, which currently rely on the cytotoxic effect of chemotherapies and/or radiotherapy and inevitably lead to high levels of toxicity and side effects in humans. The majority of available low molecular weight drugs only try to tackle disease downstream, when established in cell components at the level of expressed pathogenic proteins. Although long-favored, this therapeutic approach of treating or alleviating expressed symptoms often fails to meet therapeutic needs. For example, the high drug doses required often cause

significant side-effects (Casi & Neri, 2015; Chari, 2008), typical for chemotherapy and anti-viral drugs; and many proteins (e.g. transcription factors) are not suited to targeting by small-molecule drugs due to their nuclear location, complexity and/or lack of suitable binding sites.

Recently, an alternative approach has been developed (Beloglazova et al., 2004; Bennett et al., 2017; Bennett & Swayze, 2010; Garzon et al., 2010; Kole et al., 2012) with focus instead on the upstream catalytic targeting of disease-relevant RNAs, which include mRNAs encoding pathogenic proteins, non-coding RNAs involved in cellular signaling pathways (e.g. microRNAs) or viral genomic RNA. The advantage of RNA as a therapeutic target is recognized due to its pervasive role in macromolecular processes, including transcriptional and translational regulation, epigenetic memory (Holoch & Moazed, 2015), RNA splicing (Romero-Barrios et al., 2018) and retroviral replication (Zhang et al., 2018). Further, as RNA is the genetic material of some viruses, the RNA virus

CONTACT Elena V. Bichenkova  elena.v.bichenkova@manchester.ac.uk

 Supplemental data for this article can be accessed online at <https://doi.org/10.1080/07391102.2020.1751711>.

© 2020 The Author(s). Published by Informa UK Limited, trading as Taylor & Francis Group
This is an Open Access article distributed under the terms of the Creative Commons Attribution License (<http://creativecommons.org/licenses/by/4.0/>), which permits unrestricted use, distribution, and reproduction in any medium, provided the original work is properly cited.

genome could be selectively attacked. Key advantages of using RNA as a therapeutic target include the lack of repair mechanisms, accessibility of many RNAs in the cytoplasm and a less-intensive puckering structure with greater tertiary structural diversity than DNA, thus providing specific folding motifs as additional targets for site-specific drugs.

We have recently developed a new class of catalytic bioconjugates, as synthetic ribonucleases using amphipathic peptides, which only cleave RNA when conjugated to oligonucleotide recognition motifs (Mironova et al., 2002; Mironova, Boutorine et al., 2004; Mironova, Pyshnyi, Ivanova et al., 2004; Mironova et al., 2006, 2007; Patutina et al., 2017, 2019; Pyshnyi et al., 1997; Staroseletz, Williams et al., 2017; Williams et al., 2015). These RNA-targeting synthetic nucleases are chemically-engineered by conjugation of short, catalytically-inactive peptides with oligonucleotide recognition motif components, which range from fully- through poorly- to non-complementary to the target RNA, in order to produce novel biologically-active molecules capable of recognizing and cleaving RNA sequences quantitatively. The most remarkable feature of these novel biocatalysts is that the conjugation of peptide and oligonucleotide seems to produce a new, hybrid type of molecule (Mironova, Boutorine et al., 2004; Mironova, Pyshnyi, Ivanova et al., 2004; Mironova et al., 2006), with new properties, which are not found in nature. This synergistic combination of the individual properties of the two components yields a new catalytic entity, which is capable of catalyzing the cleavage of phosphodiester bonds in RNA under physiological conditions, with a rate enhancement factor of RNA cleavage reaching 10^8 in some cases, as compared to non-catalyzed reaction (Mironova et al., 2007). We have recently demonstrated that this type of biologically-active conjugates can selectively knock down highly-oncogenic miR-21 by irreversible cleavage and thereby down-regulate abnormal expression in lymphosarcoma cells, thus leading to a reduction in proliferative activity of tumor cells (Patutina et al., 2017, 2019).

Insight into the different binding behaviors of the catalytic and recognition elements of these novel bioconjugates is essential for rational design to control their biological behavior, and to accelerate their translational development into therapies with clinical impact. Potent, selective and irreversible catalytic cleavage of specific mRNA sequences encoding disease-relevant proteins or different micro-RNAs associated with diverse types of human pathology (e.g. cancer, inflammation, neurodegeneration) has the potential to expand the scientific boundaries of drug discovery and allow new selective therapies to develop.

Peptidyl-oligonucleotide conjugates (POCs) designed to date have the ability to cleave RNA at two different extremes: (i) either sequence-specifically (Mironova et al., 2002; Patutina et al., 2017, 2019; Pyshnyi et al., 1997; Staroseletz, Williams et al., 2017; Williams et al., 2015) by *site-directed* cleavage of the regions adjacent to the RNA hybridization sites, but in a non-catalytic manner; or (ii) non-specifically at non-complementary regions, which were located distantly from the major RNA binding region, but with a high level of catalytic turnover (Mironova, Boutorine et al., 2004; Mironova, Pyshnyi, Ivanova

et al., 2004; Mironova et al., 2006, 2007). These data provided some experimental indications that peptidyl-oligonucleotide conjugates may interact differently with the complementary and non-complementary regions of RNA sequences. Insight into the role of different structural elements of such bioconjugates in recognizing and cleaving RNA sequences is now vital, but challenging. Precise sequence-specific recognition of the target often opposes their ability to leave RNA after each cleavage event, and gain the high level of reaction by catalytic turnover, necessary for a potent drug. This study aims therefore to investigate the possible modes of the interactions of catalytic peptide and model POCs bearing 6-mer and 9-mer oligonucleotide recognition components (see **C1**, **C2** or **C3**, respectively; **Figure 1**) with both complementary and non-complementary 20-mer RNA targets using fluorescent, UV-visible and NMR spectroscopies. 2'-O-methyl oligoribonucleotide analogues were used as model RNA targets, in order to prevent any cleavage during hybridization experiments. We find that charge screening produces markedly different interactions under electrolyte conditions relevant to the intracellular environment, where high levels of monovalent cations (K^+) and low levels of divalent cations (Ca^{++}) are tightly controlled in the cytosolic domain of transcribed RNA. NMR Diffusion Ordered Spectroscopy (DOSY) illustrated self-assembly of 20 Å monomeric into 40 Å dimeric peptide-oligonucleotide complexes, which may explain the non-linear enhancement of their catalytic activity with concentration, and the possible benefit of engineering assembly.

2. Materials and methods

2.1. Materials

Reagents, of the highest quality available, were purchased from the following suppliers.

Aldrich Chemical Company, Dorset: cetyltrimethylammonium bromide; AldrithiolTM-2; triphenylphosphine; 4-(*N*, *N*-Dimethyl)aminopyridine; *N*, *N*-dimethylformamide (DMF) (anhydrous); *N*, *N*-diisopropylethylamine (anhydrous); lithium perchlorate (anhydrous); dimethyl sulfoxide (DMSO).

Novabiochem, Nottingham, UK: Boc-Arg(Tos)-OH; Boc-Gly-OH; Boc-Leu-OH.H₂O; Boc-Valine-OH; Boc-Lys (Z)-OH; HBTU and MBHA resin LL (100–200 mesh).HCl.

ACROS OrganicsTM: Water for molecular biology, DNase, RNase and Protease free.

Cambridge Isotope Laboratories, Andover, USA: Deuterated water (D₂O).

Fluorochem Ltd., Glossop: trifluoroacetic acid (TFA).

ATDBio Ltd., Southampton, UK: Oligodeoxyribonucleotides and 2'-O-methyl oligoribonucleotide analogues.

Oligodeoxyribonucleotides: 5'pTCAATC^{3'} (ON₁); 5'pTTTTCAATC^{3'} (ON₂);

The following 2'-O-methyl oligoribonucleotide analogues were used as model RNA targets, in order to prevent cleavage during the hybridization experiments:

5'GAUUGAAAAGAGGGAGAGAG^{3'} (RNA₁); 5'UUACACACACUGGGAAGUUU^{3'} (RNA₂); FAM-5'pGAUUGAAAAGAGGGAGAGAG^{3'} (FAM-RNA₁); FAM-5'pUUACACACACUGGGAAGUUU^{3'} (FAM-RNA₂).

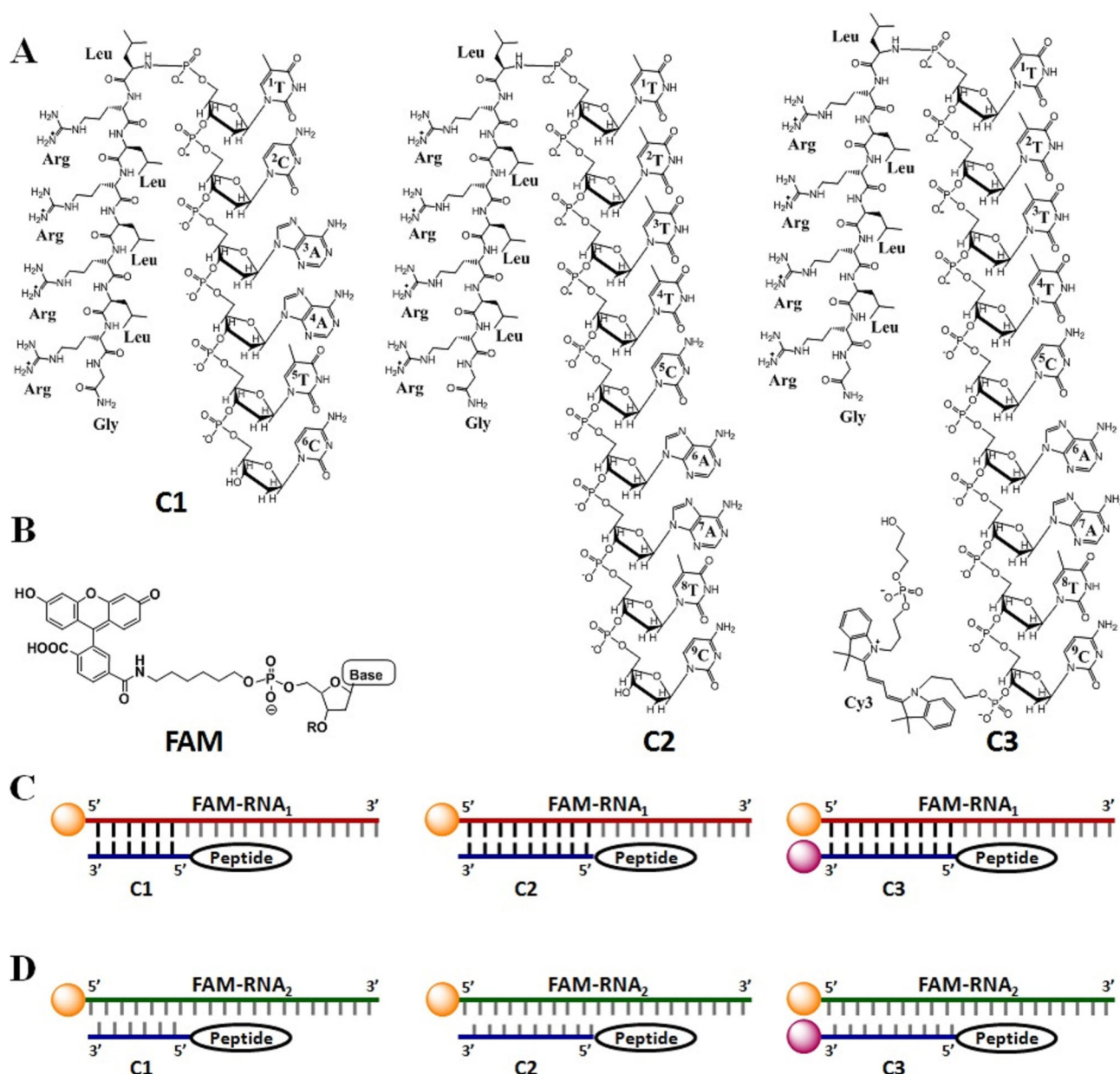


Figure 1. (A) Chemical structures of the key peptidyl-oligonucleotide conjugates **C1**, **C2** and Cy3-labelled **C3** used in the studies of the *POC-RNA* interactions. (B) Chemical structure of fluorescein (FAM) and mode of its attachment to the 5'-terminal phosphate of nucleic acid residues. (C–D) Six *POC-RNA* systems studied in the hybridization assays, which involved the conjugate NH₂-Gly-[Arg-Leu]₄-5'pTCAATC^{3'} (**C1**), NH₂-Gly-[Arg-Leu]₄-5'pTTTTCAATC^{3'} (**C2**) or Cy3-labelled NH₂-Gly-[Arg-Leu]₄-5'pTTTTCAATC^{3'}-Cy3 (**C3**) with 5'-FAM labelled complementary (C) RNA target FAM-5'pGAUUGAAAAGAGGAGAGAG^{3'} (FAM-RNA₁; red) or non-complementary (D) RNA target FAM-5'pUUACACACACUGGGAAGUUU^{3'} (FAM-RNA₂; green). The Watson-Crick base-pairs between the complementary oligonucleotide component and FAM-RNA₁ are shown aligned and indicated in black. All conjugates carry the same peptide moiety -[Leu-Arg]₄-Gly-NH₂ (black) attached at the 5'-terminal position of the oligonucleotide component (blue). The orange and pink spheres represent the attached fluorescein (FAM) and indocarbocyanine (Cy3) dyes, respectively.

2.2. Analytical methods and instrumentation

Reversed phase HPLC. HPLC purification of compounds was performed using an Agilent 1100 system fitted with a thermostated column compartment, a quaternary pump with solvent degasser, and a diode-array detector module for multi-wavelength signal detection using an Agilent 1100 series of UV-visible and a fluorescent detector module. The system had a manual Rheodyne injector, and the instrument was operated through a PC running Agilent HPLC 2D ChemStation Software. Depending on the purpose indicated, the columns used were: semi-prep Phenomenex Luna 5 μ m

C18 column (250 \times 10 mm), or analytical Phenomenex Luna, 5 μ m C18 column (250 \times 4.6 mm).

NMR spectroscopy. 1D NMR (¹H and ¹³C) and 2D NMR (¹H-¹H-NOESY, ¹H-¹H-COSY, ¹H-¹H-TOCSY and ¹H-¹³C HSQC) spectra were recorded using Bruker Avance II + spectrometers operating at proton frequencies of 400 or 500 MHz. ³¹P NMR spectra were recorded using either a Bruker 300 MHz (Avance-300) spectrometer or Bruker Avance II + spectrometers (400 MHz) operating at phosphorus frequencies of 121.5 MHz or 162 MHz, respectively. In all cases, spectra were acquired and processed using Bruker software TopSpin® v2.0 or v2.1.

1D ^1H NMR data were collected using 64 transients into 65 k data points over a spectral width of 8 kHz (400 MHz spectrometer) or 10 kHz (500 MHz spectrometer), with a relaxation delay of 2.4 s between scans. ^{31}P NMR data were collected into 64 K data points over a spectral width of 48 KHz. For each spectrum up to 4095 transients were acquired, with 2 s relaxation delay between scans. Processing involved multiplication by an exponential window function prior to Fourier transform and phase correction. In all cases, the spectrometers were equipped with Microsoft Windows XP Professional running TopSpin® NMR software (Version 2.0 or 2.1) for acquiring and processing NMR data. Chemical shifts (δ) are reported in parts per million (ppm) with peak positions reported relative to trimethylsilyl-2,2,3,3-tetra-deuteropropionic acid (0.00 ppm) and trimethyl phosphate (TMP; 3.1 ppm) internal standards for ^1H NMR and ^{31}P NMR experiments, respectively.

Two-dimensional ^1H - ^1H COSY NMR data were collected with quadrature detection into 2048 complex data points for 512 or 1024 t_1 increments with a number of transients appropriate for the sample concentration being acquired for each t_1 increment. Data were acquired over 3.2 KHz (400 MHz spectrometer) or around 4 KHz (500 MHz spectrometer) with optimized spectral width for each sample from the 1D ^1H spectrum, and with 1.64 s relaxation delay.

2D ^1H NOESY spectra were recorded using 500 MHz Bruker Avance+II spectrometer using *noesyprf2gpph* pulse program, with water pre-saturation and a phase sensitive acquisition mode State-TPPI. Spectra were collected into 2048 complex points in the t_2 dimension and 512 complex points in the t_1 dimensions. The mixing time was 0.5 s, and the relaxation delay between scans was 1.82 s. The spectral width was set to 8.0 ppm in both dimensions, and the sample spinning was turned off. The spectra were processed using TopSpin® 2.1 by applying Fourier transformation for both dimensions using QSIN window function after zero-filling.

Data reported use the following convention: chemical shift (splitting patterns, integrated intensity, and assignment). Abbreviations used for splitting patterns are: s (singlet), d (doublet), t (triplet), q (quartet), m (multiplet), dd (doublet of doublets), dt (doublet of triplets), br (broad), obs (observed).

^1H DOSY experiments (Bichenkova et al., 2017; Valentini et al., 2004) were carried out on the 400 MHz Bruker Avance+II spectrometer, using 5 mm MIC Z121725/0001DOSY z-diffusion probe with fixed $^1\text{H}/\text{X}$ configuration and ^2H lock to generate a gradient strength of 30 Gauss/cm/A. The combination of the DIFF30L probe with the 40 Amp gradient current amplifier (GREAT 40) allowed to produce a field strength up to maximum of 1200 Gauss/cm. The pulse program used was *diffste*, and the experiments were run at room temperature. The gradient (g), the length of the gradient pulse (δ) and the diffusion time (Δ) were calibrated for each experiment using TopSpin® DOSY script (*diff*). An array of experiments with different combinations of the three parameters was run to obtain sufficient signal attenuation. At the parameterization step, each experiment was run over 16 scans and 16 gradient steps. The typical value for the gradient field (g)

was 400 Gauss/cm, whereas the optimal values for the gradient duration (δ) and diffusion time (Δ) were 35 ms and 0.8 ms, respectively. Once the sufficient signal attenuation was achieved, the diffusion measurements were carried out using the original Bruker pulse sequences. The gradient pulse length and the diffusion time were kept at fixed values while gradually increasing the gradient strength. In each DOSY experiment, a series of 56 spectra were collected into 128 K data points, using a linear gradient ramp. The resulting FIDs were processed using MestReNova, and the diffusion coefficients and hydrodynamic radius were calculated by CONTIN algorithm (Provencher, 1982a, 1982b; Valentini et al., 2004).

Mass spectrometry. Mass spectra of the synthesized peptides and their oligonucleotide conjugates were recorded at the Manchester Interdisciplinary Biocentre (MIB, University of Manchester) using a Matrix Assisted Laser Desorption/Ionization-Time of Flight-/Time of flight (MALDI-ToF/ToF) mass spectrometer (Ultraflex II®) with pulsed nitrogen laser of wave length 337 nm and Voyager software. Some MALDI-ToF experiments were carried out for us by EPSRC National Mass Spectrometry Service Centre (Swansea University, Swansea). To record MALDI-ToF mass spectra, a $1\ \mu\text{g}/\mu\text{L}$ stock solution of a sample was prepared in water. For the peptide samples, gel matrix solutions were prepared by dissolving 2,5-dihydroxybenzoic acid in a mixture of solvent containing MeCN:water:TFA at 50:50:1 ratio, respectively, to obtain 10 mg/ml final concentrations. To record MALDI-ToF mass spectra for the oligonucleotide conjugates, α -cyano-4-hydroxycinnamic acid matrix and a solvent (1:1 mixture of MeCN and water) were used to avoid possible hydrolysis of the phosphoramidate bond by the TFA. A $0.5\ \mu\text{L}$ sample was pipetted and spotted on to a MALDI sample plate and allowed to dry. The spotted samples were then covered using $0.5\ \mu\text{L}$ matrix.

Sample quantification for hybridization experiments. The concentrations of oligonucleotides, 2'-O-methyl oligoribonucleotide analogues and oligonucleotide conjugates in stock solutions were measured by taking small aliquots (typically $2\ \mu\text{L}$; in triplicate) followed by the addition of appropriate volume of de-ionized water to obtain the final volume of 1 mL, when UV absorbance at 260 nm was measured, which was then used to estimate both the concentration of the test sample and the concentration of the original stock solution using the Beer-Lambert Law:

$$A_{260} = \epsilon_{260} \times C \times L$$

where A_{260} is UV absorbance measured at 260 nm; ϵ_{260} is the millimolar extinction coefficient of the corresponding oligonucleotide at 260 nm ($\text{mM}^{-1}\cdot\text{cm}^{-1}$), C is the concentration of the sample (mM) and L is the pathlength of the cuvette (cm). The millimolar extinction coefficients for oligonucleotides and their analogues were calculated using an online commercial (ATDbio Ltd.) oligonucleotide analyzer,¹ which evaluates extinction coefficients based on the principle of the nearest neighbor thermodynamic model. The estimated ϵ_{260} values for conjugates **C1** and **C2** were found to be 56.9 and $81.2\ \text{mM}^{-1}\cdot\text{cm}^{-1}$, respectively. In the case of fluorescently-labeled conjugate **C3** and RNA targets (FAM-RNA₁ and

FAM-RNA₂), the millimolar extinction coefficients were calculated by taking into account the millimolar extinction coefficients of free FAM ($\epsilon_{260} = 20.9 \text{ mM}^{-1} \text{ cm}^{-1}$) and Cy3 ($\epsilon_{260} = 4.93 \text{ mM}^{-1} \text{ cm}^{-1}$).² The resulting ϵ_{260} values of the fluorescently-labeled analogues were $86.13 \text{ mM}^{-1} \cdot \text{cm}^{-1}$ for **C3**, $244.6 \text{ mM}^{-1} \cdot \text{cm}^{-1}$ for FAM-RNA₁ and $215.3 \text{ mM}^{-1} \cdot \text{cm}^{-1}$ for FAM-RNA₂.

All stock solutions were additionally purified by gel filtration chromatography using IllustraTM NAP disposable columns prepacked with Sephadex G-25 (DNA grade resin) to remove any possible traces of counter cations from peptidyl-oligonucleotide conjugates, RNA and peptide samples.

UV-visible spectroscopy. UV-visible spectroscopy measurements were carried out using a Cary-4000 UV-Visible spectrophotometer from Varian (Australia) connected to a Cary Peltier temperature controller, operating under Varian Cary WinUV software. All spectra were recorded between 200 to 900 nm at 5 °C using 1 cm pathlength matched quartz cuvettes. Hybridization of the oligonucleotide conjugates **C1**, **C2** and **C3** with 20-mer RNA target (FAM-RNA₁ or FAM-RNA₂) were studied in 50 mM Tris-HCl, 200 mM KCl, and 0.5 mM EDTA at pH 7.0. Initially, the UV-visible spectra of the oligonucleotide conjugates (2.5 μM) alone were measured in buffer at 5 °C (λ_{max} , 260 nm). The target RNA was then added to achieve 2.5 μM concentration in the cuvette, and spectra were taken until no further change occurred.

Fluorescence spectroscopy. Fluorescence excitation and emission spectra were recorded in 1 cm pathlength quartz cuvettes at 5 °C using a Cary-Eclipse fluorescence spectrophotometer fitted with Cary Peltier-thermostat cuvette holder. The instrument was operated with Cary Eclipse software for Windows. Hybridization of the oligonucleotide conjugates **C1–C3** with complementary 20-mer RNA target (FAM-RNA₁ or FAM-RNA₂) were studied either in Tris buffer (50 mM Tris-HCl, 200 mM KCl, and 0.5 mM EDTA at pH 7.0) or in de-ionized water. First, the emission spectra of the free fluorescently-labeled component (either FAM-RNA₁ or FAM-RNA₂; 5 μM) were measured at 5 °C following excitation at 495 nm. Then, the second component (**C1**, **C2** or **C3**) was added to reach the final conjugate concentration of 5 μM in the cuvette, to achieve 1:1 molar ratio of both components. The emission spectra of the complex formed were then recorded following excitation at 495 nm. In the independent experiments with the dually labeled system, the emission spectrum of **C3** (2.5 μM) was first recorded either in water or in Tris buffer on excitation at 552 nm, followed by addition either FAM-RNA₁ or FAM-RNA₂ to achieve 2.5 μM final concentration in the cuvette. The binding between conjugates and RNA sequences was monitored by recording fluorescence spectra at 570 nm (for Cy3 emission) following excitation at 552 nm.

Melting curves. Melting temperature experiments were performed in 1 cm pathlength quartz cuvettes using a Cary-4000 UV-visible spectrophotometer fitted with Cary Peltier-thermostat cuvette holder. Thermal denaturation experiments monitored at 260 nm (oligonucleotide absorbance), 495 nm (FAM absorbance) and/or 550 nm (Cy3 absorbance) were recorded between 5 and 90 °C, at a rate of 0.5 or

0.1 °C/min with a data interval of 0.5 or 0.1 °C. The melting temperature, T_m , is defined as the temperature corresponding to the half-transition of the thermal denaturation process of the duplex. The T_m values were calculated as the maxima of the first-order derivatives of the melting curves using Cary software.

2.3. Peptide synthesis

Catalytic peptide [Leu-Arg]₄-Gly-NH₂ was synthesized by manual solid-phase Boc strategy using MBHA.HCl resin. 4-methylbenzhydramine hydrochloride salt resin (1.02 g, MBHA.HCl (0.59 mEq amine/g, $\sim 0.602 \text{ mmol}$)) was washed with DCM, neutralized with DIPEA/DCM (1:19, ca. 12 mL) for 5 min and left to swell in DCM over two days, re-washed with DCM and DMF, and the first Boc-protected amino acid residue, Boc-Gly-OH, was added to perform the coupling procedure as described below. At each coupling step, 1.81 mmol of the Boc-amino acid to be coupled (3.0 eq. relative to resin-bound amine) was pre-activated for 3–5 min in a small vial by combining it with O-benzotriazole-N,N,N',N'-tetramethyluronium-hexafluoro-phosphate (HBTU, 3 eq. relative to resin-bound amine) and diisopropylethylamine (DIPEA, 9 eq. relative to resin-bound amine) in 10 mL of DMF and added to the glass vessel containing resin. The reaction vessel was shaken for 40 min, washed with DMF (2 \times 15 mL) and DCM (2 \times 15 mL). The resulting mixed Boc-aminoacyl polymer was assessed with ninhydrin using the Kaiser test (Stewart & Young, 1979). The aminoacyl resin was then treated with TFA/DCM (1:1) for 2 min, again with TFA/DCM (1:1) for 30 min, washed with DCM ($\times 4$), neutralized with DIPEA/DCM (1:19) for 5 min and finally washed with DCM and DMF to complete the coupling cycle. The same cycle was repeated for coupling the remaining amino acid residues to obtain the desired sequence [Leu-Arg]₄-Gly-NH₂. After completion of the final coupling cycle, the peptide resin was washed twice with DCM followed by MeOH and dried.

The dried resin with the attached peptide chain was placed in a reactor equipped with a Teflon-coated stirring bar, when p-cresol (0.75 g) and of thiocresol (0.25 g) scavengers were added. The reactor was closed, connected to the apparatus and cooled down in an ice bath to 0 – 4 °C, when HF (15 mL) was distilled under vacuum into the reaction vessel and stirred for 2 h. The HF was evaporated under vacuum at low temperature (4 °C). The cleaved peptide and resin were suspended in diethyl ether to precipitate the peptide, which was washed with diethyl ether and then with EtOAc (2 \times 30 mL) to remove the remaining scavengers. The peptide was extracted with 20% acetic acid ($\times 3$), followed by 80% acetonitrile to ensure the complete removal of the peptide from the resin. Finally, the solution was lyophilized to give $\sim 500 \text{ mg}$ of crude yield of pale green solid.

The crude peptide was purified by reversed phase HPLC using a Phenomenex Luna C-18 column (5 μm ; 250 mm \times 10 mm) and eluents **A** (0.1% TFA and 1% CH₃CN in water) and **B** (0.1% TFA and 1% water in CH₃CN). The absorbance was monitored at 220 nm, and the following elution gradients were applied: 0% **B** to 32% **B** in 40 min. The peptide

fractions eluted at 34.9–36.0 min were lyophilized to produce the peptide as a trifluoroacetic acid salt (reaction yield: 21%). The chemical structure of the peptide [Leu-Arg]₄-Gly-NH₂, along with the atom numbering used for the proton signal assignment, is shown in the [Supplementary Figure S1](#) (see [Supplementary Material](#)).

Peptide [Leu-Arg]₄-Gly-NH₂. MALDI-TOF: $m/z = 1151.9$ for $[M + H]^+$ (M.W. = 1150.8 calculated for C₅₀H₉₈N₂₂O₉). ¹H NMR (400 MHz, D₂O, 5.0 °C, 1.5 mM, TSP): δ_H 4.39 (1H, apparent t, *J* 7.0, ^{2/4/6/8}Arg 2-H), 4.28–4.38 (6H, m, ^{3/5/7}Leu 2-H, 3 of ^{2/4/6/8}Arg 2-H), 3.99 (1H, apparent br m, ¹Leu 2-H), 3.95 (1H, d, *J* 17.2, ⁹Gly 2-HH), 3.89 (1H, d, *J* 17.2, ⁹Gly 2-HH), 3.18–3.25 (8H, m, ^{2/4/6/8}Arg 5-HH), 1.51–1.94 (28H, m, ^{1/3/5/7}Leu 3-HH, ^{1/3/5/7}Leu 4-H, ^{2/4/6/8}Arg 3-HH, ^{2/4/6/8}Arg 4-HH), 0.93–0.98 (15H, m, 2 × ¹Leu 5-H₃, 1 × ³Leu 5-H₃, 1 × ⁵Leu 5-H₃, 1 × ⁷Leu 5-H₃), 0.87–0.91 (9H, m, 1 × ³Leu 5-H₃, 1 × ⁵Leu 5-H₃, 1 × ⁷Leu 5-H₃).

2.4. Coupling of the peptide to oligonucleotide

Prior to coupling of the peptide [Leu-Arg]₄-Gly-NH₂ to the 5'-terminal phosphate group of the oligonucleotide, the latter was converted into the N-cetyl-N,N,N-trimethylammonium salt, soluble in DMSO, as described earlier (Staroseletz, Williams et al., 2017; Williams et al., 2015). The N-cetyl-N,N,N-trimethylammonium salt of the oligonucleotide (0.12 μmol) was dissolved in anhydrous DMSO (~ 60 μL) and treated with an excess of activating agents: 2,2'-dipyridyl disulfide (10 mg, 45.5 μmol) and triphenylphosphine (10 mg, 38.1 μmol) for 5 min at room temperature followed by addition of N,N-dimethylaminopyridine (5 mg, 41 μmol) for another 10 min. Anhydrous DMSO (20 μL) and 4-(dimethylamino)pyridine (3 mg, 24.6 μmol) were added to a separate tube containing oligopeptide (1.4 mg, 1.2 μmol), and the resulting solution was transferred into the activated oligonucleotide solutions. The reaction mixture was incubated at 40 °C for 3 h, followed by precipitation with 4% LiClO₄ in acetone as described in (Staroseletz, Williams et al., 2017; Williams et al., 2015).

The crude conjugate was purified by reversed phase HPLC using a semi-prep Phenomenex Luna column C18 (5 μm; 250 × 10 mm) and mobile phases **A** (0.05 M LiClO₄ in water) and **B** (0.05 M LiClO₄ in 100% acetonitrile). The following gradient for RP-HPLC purification of the conjugates was applied: 100% A for 3 min, 0% B to 50% B in 30 min. The eluted fractions were monitored using UV-visible detection at 220, 260 nm and 552 nm (for **C3**), characteristic absorbance of the peptide, oligonucleotide moiety and the attached Cy3 dye, respectively. The desired conjugates **C1-C3** eluted at a longer retention time than their corresponding oligonucleotide components 6-mer ON₁ (16 min), 9-mer ON₂ (18 min). The retention times of the synthesized conjugates were 23.5 min, 25 min and 24 min for conjugates **C1**, **C2** and **C3**, respectively. Conventional numbering and nomenclature used for assignment of oligonucleotide ¹H NMR signals are shown in [Supplementary Figure S2](#) (see [Supplementary Material](#)).

Conjugate C1. MALDI-TOF: $m/z = 2966.0$ for $[M + 2H]^+$ (M.W. = 2965.10, calculated for C₁₀₈H₁₇₃N₄₂O₄₅P₆ [M + H]⁺). ¹H NMR (500 MHz, D₂O, 5.0 °C); δ_H 8.36 (1H, s, ⁴A 8-H), 8.23 (1H,

s, ³A 8-H), 7.91 (1H, s, ³A 2-H), 7.85 (1H, s, ⁴A 2-H), 7.81 (1H, d, *J* 7.6, ⁶C 6-H), 7.66 (1H, s, ¹T 6-H), 7.56 (1H, d, *J* 7.5, ²C 6-H), 7.29 (1H, s, ⁵T 6-H), 6.24 (1H, apparent t, *J* 6.5, ⁶C H-1'), 6.21 (1H, m, ¹T H-1'), 6.19 (1H, m, ⁴A H-1'), 6.06 (1H, m, ²C H-1'), 6.03 (1H, m, ⁵T H-1'), 6.02 (1H, m, ³A H-1'), 6.00 (1H, d, *J* 7.6, ⁶C 5-H), 5.96 (1H, d, *J* 7.5, ²C 5-H), 4.97 (1H, m, ³A H-3'), 4.80 (1H, m, ⁵T H-3'), 4.79 (1H, m, ¹T H-3'), 4.73 (1H, m, ²C H-3'), 4.54 (1H, apparent dt, *J* 6.0, 4.0, ⁶C H-3'), 4.46 (1H, m, ⁴A H-3'), 3.87–4.36 (25H, m, 18H from oligonucleotide H-4'/H-5'/H-5'' protons and 7H from peptide protons including 3 of ^{3/5/7}Leu 2-H, 4 of ^{2/4/6/8}Arg 2-H), 3.95 (1H, d, *J* 17.2, ⁹Gly 2-HH), 3.89 (1H, d, *J* 17.2, ⁹Gly 2-HH), 3.65 (1H, apparent q, *J* 7.3, ¹Leu 2-H), 3.12–3.23 (8H, m, ^{2/4/6/8}Arg 5-HH), 2.77 (1H, m, ⁴A H-2''), 2.77 (1H, m, ³A H-2''), 2.74 (1H, m, ⁴A H-2'), 2.63 (1H, m, ³A H-2'), 2.45 (1H, m, ¹T H-2'), 2.37 (1H, m, ⁶C H-2''), 2.36 (1H, m, ⁵T H-2''), 2.27 (1H, m, ¹T H-2'), 2.27 (1H, m, ²C H-2''), 2.26 (1H, m, ⁶C H-2'), 2.14 (1H, m, ⁵T H-2'), 1.51–1.94 (26H, m, ^{3/5/7}Leu 3-HH, ^{1/3/5/7}Leu-4H, ^{2/4/6/8}Arg 3-HH, ^{2/4/6/8}Arg 4-HH), 1.90 (3H, s, ¹T 5-CH₃), 1.79 (1H, m, ²C H-2'), 1.65 (3H, s, ⁵T 5-CH₃), 1.41–1.48 (2H, m, ¹Leu 3-HH), 0.80–0.94 (24H, m, ^{1/3/5/7}Leu 5-CH₃). ³¹P NMR (121 MHz, 2.5 mM, D₂O, 22 °C): δ_P 6.9 (NP), 0.4, 0.2, 0.1, 0.0, 0.0.

Conjugate C2. MALDI-ToF: $m/z = 3876$ for $(M + H)^+$; (M.W. = 3875.23, calculated for C₁₃₈H₂₁₁N₄₈O₆₆P₉). ¹H NMR (500 MHz, D₂O); δ_H 8.30 (1H, s, ⁷A 8-H), 8.14 (1H, s, ⁶A 8-H), 7.93 (1H, s, ⁶A 2-H), 7.89 (1H, s, ⁷A 2-H), 7.80 (1H, d, *J* 7.6, ⁹C 6-H), 7.72 (1H, s, ¹T 6-H), 7.70 (3H, m, ²⁻⁴T 6-H), 7.51 (1H, d, *J* 7.5, ⁵C 6-H), 7.29 (1H, s, ⁸T 6-H), 6.25 (4H, m, ¹⁻⁴T H-1'), 6.24 (1H, m, ⁷A H-1'), 6.23 (1H, m, ⁵C H-1'), 6.22 (1H, m, ⁹C H-1'), 6.05 (1H, m, ⁶A H-1'), 6.02 (1H, m, ⁸T H-1'), 5.99 (1H, d, *J* 7.6, ⁹C 5-H), 5.88 (1H, d, *J* 7.5, ⁵C 5-H), 4.89 (3H, m, ²⁻⁴T H-3'), 4.83 (1H, m, ¹T H-3'), 4.81 (1H, m, ⁸T H-3'), 4.69 (1H, m, ⁵C H-3'), 4.54 (1H, apparent dt, *J* 6.0, 4.0, ⁹C H-3'), 4.48 (1H, m, ⁷A H-3'), 3.87–4.40 (34H, m, 27H from oligonucleotide H-4'/H-5'/H-5'' protons and 7H from peptide protons including 3 of ^{3/5/7}Leu 2-H, 4 of ^{2/4/6/8}Arg 2-H), 3.95 (1H, d, *J* 17.2, ⁹Gly 2-HH), 3.89 (1H, d, *J* 17.2, ⁹Gly 2-HH), 3.65 (1H, apparent q, *J* 7.3, ¹Leu 2-H), 3.10–3.25 (8H, m, ^{2/4/6/8}Arg 5-HH), 2.83 (1H, m, ⁶A H-2'), 2.78 (1H, m, ⁷A H-2''), 2.53 (4H, m, ¹⁻⁴T H-2'), 2.40 (1H, m, ⁵C H-2''), 2.43–2.28 (6H, m, which include 2H from ⁸T H-2'' and ⁹C-H2'', and 4H from ¹⁻⁴T H-2''), 2.24 (1H, m, ⁹C H-2'), 2.21 (1H, m, ⁶A H-2''), 2.18 (1H, m, ⁵C H-2'), 2.13 (1H, m, ⁸T H-2'), 1.92, 1.90, 1.89 and 1.88 (12H, s, ¹⁻⁴T 5-CH₃), 1.74–1.90 (14H, m, ^{3/5/7}Leu 3-HH and ^{2/4/6/8}Arg 3-HH), 1.49–1.75 (12H, m, ^{1/3/5/7}Leu-4H and ^{2/4/6/8}Arg 4-HH), 1.90 (3H, s, ⁵T 5-CH₃), 1.65 (3H, s, ⁸T 5-CH₃), 1.41–1.48 (2H, m, ¹Leu 3-HH), 0.80–0.94 (24H, m, ^{1/3/5/7}L 5-CH₃). ³¹P NMR (121 MHz, in D₂O, 22 °C): δ_P 6.94 (NP), 0.37, 0.29–0.24 (7P, m).

Conjugate C3. MALDI-ToF: $m/z = 4524$ for $(M + 4H)^+$; (M.W. = 4521, calculated for C₁₇₀H₂₅₄N₅₀O₇₄P₁₁ (M + H)⁺). Conjugate **C3** showed similar ¹H resonances signals to that of conjugate **C2** both for the oligonucleotide and the peptide components. The characteristic signals arising from the covalently attached Cy3 dye include: ¹H NMR (500 MHz, D₂O); δ_H triplet at 8.4 (1H, t, *J* 12.5 Hz, Ar-H5); 7.5–7.2 (8H, m, 7xAr-H & ⁸T-H6); 6.37 (2H, d, *J* 13.4 Hz, H-10 & 12); 6.2 (1H, t, *J* 13.2 Hz, H-11); 3.8–4.0 (8H, m, H-22,27,29&30); 3.4–3.6 (4H,

t, $J = 6.5$ Hz, H-24&32); 1.5 – 2.0 (18H, m, $4 \times \text{CH}_3$ & H-23, 28 & 31).

^1H NMR spectra of the conjugates **C1**, **C2** and **C3** (400 MHz, Bruker) are given in Supplementary Figures S3, S4 and S5, respectively (see [Supplementary Material](#)).

2.5. RNA cleavage assays

Preparation of substrate RNAs. RNA HIV-1 was prepared by in vitro transcription with T7 RNA polymerase using Fok I – linearized plasmid pHIV-1 (Milligan & Uhlenbeck, 1989). The reaction was carried out in 300 μL of 40 mM Tris-HCl, pH 7.5, containing 6 mM MgCl_2 , 2 mM spermidine, 10 mM sodium chloride, 10 mM dithiothreitol, 1 mM of each NTP, 30 μg of DNA template, and 100 U T7 RNA polymerase, for 2 h at 37 °C. The reaction was quenched by phenol/chloroform (1:1, v/v) extraction, followed by ethanol precipitation. After centrifugation, RNA precipitate was rinsed twice with 80% ethanol and dissolved in water.

HIV-1 RNA transcript was dephosphorylated using bacterial alkaline phosphatase BAP (Fermentas) according to a described protocol (Silberklang et al., 1979). The reaction mixture, 50 μL of 50 mM Tris-HCl, pH 8.5, containing 1 mM EDTA, 0.2% SDS, 2% formamide, 2.5 mM DTT, 0.1 A_{260} in vitro transcript of RNA HIV-1 and 2 U of bacterial alkaline phosphatase was incubated at 37 °C for 1 h. BAP was added to the reaction mixture at 0 and 30 min incubation time. The reaction was quenched by phenol/chloroform (1:1, v/v) extraction followed by extraction of water phase with ethyl ester and ethanol precipitation.

RNA 5'-labeling. 5'-End labeling of RNA HIV-1 was carried out using [γ - ^{32}P]-ATP and T4 polynucleotide kinase (Fermentas) according to a described protocol (Silberklang et al., 1979). ^{32}P -labeled RNAs were isolated by electrophoresis in 12% denaturing polyacrylamide gel with 8 M urea. RNAs were visualized by autoradiography using X-ray film. ^{32}P -labelled RNAs were eluted from the gel with 300 μL 0.3 M sodium acetate, pH 5.5 followed by ethanol precipitation.

Ribonuclease activity assay. The reaction mixture (10 μL) was prepared in such a way to contain the following components at the stated final concentrations: 50,000 cpm 5'-[^{32}P]-labelled RNA, one of the oligonucleotide-peptide conjugates (**C1** or **C2**) at concentration either 10 μM or 50 μM in 50 mM Tris-HCl buffer, pH 7.0, 0.2 M KCl and 1 mM EDTA, in the presence of 100 $\mu\text{g mL}^{-1}$ RNA carrier. The mixtures were incubated at 37 °C (for various times) and quenched by precipitation of RNA with 2% lithium perchlorate in acetone (150 μL). RNA was collected by centrifugation and dissolved in loading buffer (6 M urea, 0.025% bromophenol blue, 0.025% xylene cyanol). RNA and RNA cleavage products were resolved in 12% polyacrylamide/8 M urea gel using TBE (100 mM Tris-borate, pH 8.3, 2 mM EDTA) as a running buffer. To identify cleavage sites, an imidazole ladder and G-ladder produced by partial RNA cleavage with 2 M imidazole buffer (pH 7.0) and with RNase T1, respectively, were run in parallel. Quantitative data were obtained by counting using Molecular Imager FX (Bio-Rad, USA). The total extent of RNA cleavage and extent of RNA cleavage at specific sites were

determined as a ratio of radioactivity measured in the RNA fragment(s) to the total radioactivity applied onto the gel.

3. Results and discussion

3.1. Conjugate design

Peptidyl-oligonucleotide conjugates **C1–C3** were designed to report interactions with target RNA by fluorescence, UV-visible and NMR studies (see [Figure 1](#) for chemical structures and nomenclature, and [Supplementary Figure S6](#) for oligonucleotide sequences). FAM was used as a dye for fluorescent labeling of the model complementary (FAM-RNA₁) and non-complementary (FAM-RNA₂) targets ([Figure 1\(B\)](#)). Indocarbocyanine dye (Cy3) was also used as a fluorescent tag at the 3'-terminal position of the 9-mer conjugate to produce fluorescently labelled conjugate **C3**. Fluorescein has an absorption maximum around 495 nm and fluorescence emission maximum at 520 nm, whereas Cy3 has absorption maxima around 550 nm and emission maxima at 570 nm. Change in fluorescence of the two fluorophores should report binding between **C3** and the FAM-labelled RNA sequences and provide useful indications of the mode of interactions at least by quenching, if not by Förster Resonance Energy Transfer (FRET). FAM and Cy3 often act as a *Donor-Acceptor* couple (Chen et al., 2010; Olejko et al., 2016; Olejko & Bald, 2017; Tsourkas et al., 2003; Zhao et al., 2010), as the fluorescence emission region of FAM (480–600 nm) substantially overlaps with the excitation region of Cy3 (470–570 nm).

The conjugates had differences in overall charge, whereas the peptide fragment was identical throughout. The 9-mer **C2** conjugate ($\text{NH}_2\text{-Gly-}[\text{Arg-Leu}]_4\text{-}^5\text{pTTTTCAATC}^3$) contained 3 additional nucleotide residues (**dTTT-**) as compared to the 6-mer **C1** conjugate ($\text{NH}_2\text{-Gly-}[\text{Arg-Leu}]_4\text{-}^5\text{pTCAATC}$), and thus carried the increased net negative charge (overall charge of (-5) for **C2** cf (-2) for **C1**). Conjugate **C3** ($\text{NH}_2\text{-Gly-}[\text{Arg-Leu}]_4\text{-}^5\text{pTTTTCAATCp}^3\text{-Cy3}$) was the structural analogue of **C2**, but carried the 3'-terminal Cy3 fluorescent label, leading to an additional increase in its net charge to attain (-6) for this fluorescently-labelled sequence.

3.2. Conjugate ribonuclease activity

Ribonuclease activities of the conjugates **C1** and **C2** were confirmed and compared in *back-to-back* studies against 5'-[^{32}P]-RNA-HIV-1 ([Figure 2\(A\)](#)), which does not contain regions that are fully complementary to the oligonucleotide components of the conjugates. The secondary structure of HIV-RNA-1 is shown in [Figure 2\(B\)](#), with red arrows indicating the major sites of RNA cleavage by **C1** and **C2** conjugates, whereas the total extent of 5'-[^{32}P]-RNA-HIV-1 cleavage is summarized by a diagram in [Figure 2\(C\)](#).

Overall efficiency of 5'-[^{32}P]-RNA-HIV-1 cleavage was found to be 30% and 37% for **C1** and **C2**, respectively, at 10 μM conjugate concentration. An increase of the conjugate concentrations to 50 μM led to the enhancement of the overall cleavage efficiency to 50% for **C1**, whereas the efficiency of its elongated analogue **C2** reached 100% over 24 h.

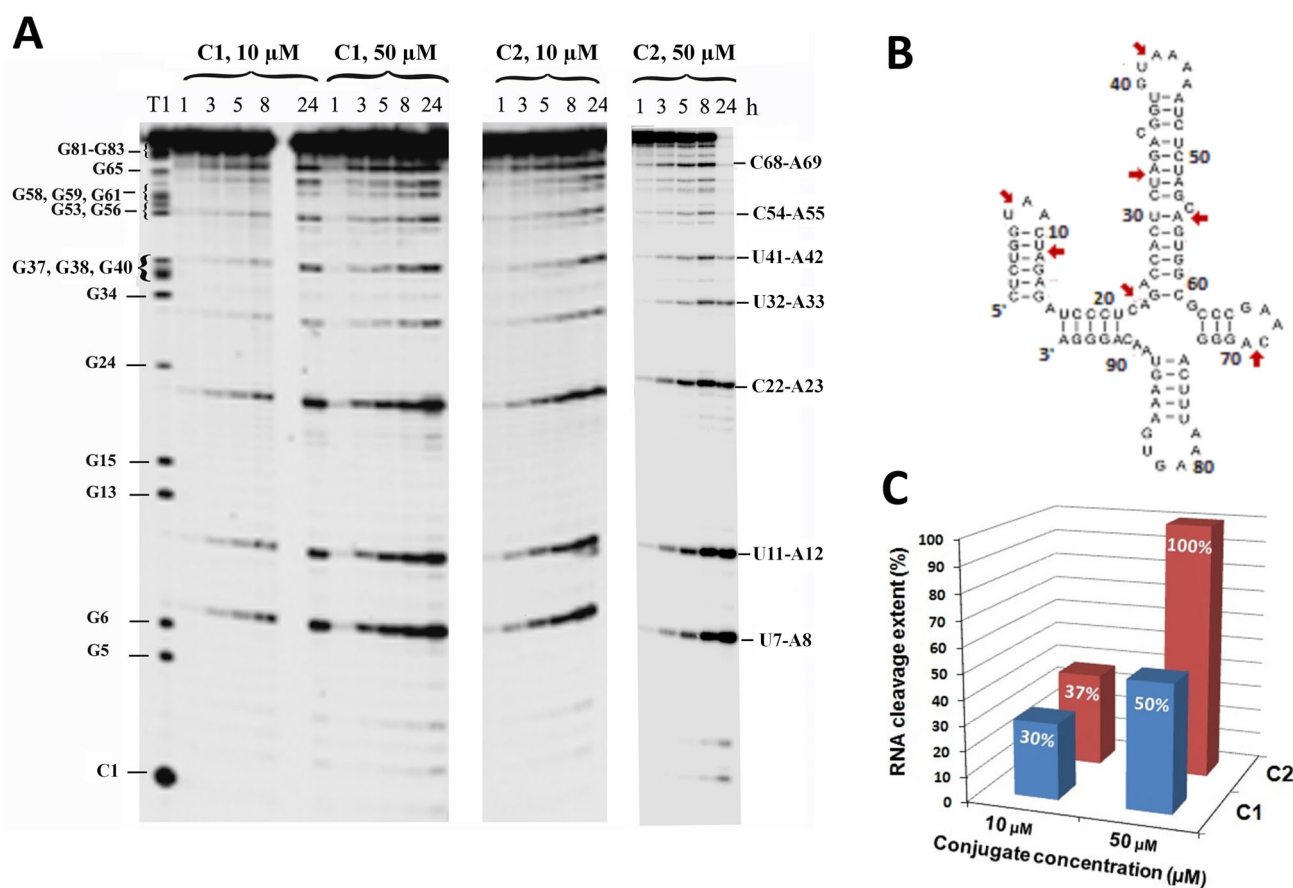


Figure 2. Analysis of the cleavage products of the 5'-[³²P]-RNA-HIV-1 by **C1** and **C2** conjugates. (A) Autoradiograph of the denaturing 12% polyacrylamide/8 M urea gel after electrophoresis of 5'-[³²P]-RNA-HIV-1 cleavage products. *Lane T1*: partial RNA digestion with RNase T1 in denaturing conditions. *Lanes 1, 3, 5, 8 and 24*: 5'-[³²P]-RNA-HIV-1 incubated in the presence of conjugates **C1** and **C2** over different periods of time. The conjugate type and incubation time are shown on the top. Reaction conditions: 5'-[³²P]-RNA-HIV-1 (1 μM) was incubated at 37 °C in the presence of conjugates at 10 μM or 50 μM concentration in 50 mM Tris-HCl, pH 7.0, 0.2 M KCl, 1 mM EDTA and in the presence of 100 μg/mL of RNA carrier. The cleavage sites produced by RNase T1 and conjugates **C1** and **C2** are shown on the left and right, respectively. (B) Secondary structure of HIV-RNA-1. Red arrows indicate the major site of RNA cleavage by **C1** and **C2** conjugates. (C) Total extent of 5'-[³²P]-RNA-HIV-1 produced by **C1** (blue) and **C2** (red) conjugates at 10 μM or 50 μM concentration (based on the data obtained in (A)).

Analysis of the RNA digestion products showed that the **C1** and **C2** conjugates cleaved 5'-[³²P]-RNA-HIV-1 predominantly at Pyr-A sites. Indeed, C-A and U-A positions were cleaved more efficiently than C-G and U-G sites. Pyr-A motifs located within loops, bulge-loops and/or junctions seemed to represent the major cleavage sites (i.e. U7-A8, U11-A12, C22-A23, U41-A42, C54-A55, C68-A69; indicated by red arrows in Figure 2(B)). In contrast, the Pyr-G motifs and the sites located within stem regions were cleaved less efficiently (e.g. U32-A33 > C60-G61, C64-G65, U77-A78, C90-A91 ≫ U51-A52), and were detected mainly at higher conjugate concentrations (50 μM), thus signifying the lower propensity of these sites toward cleavage by this class of conjugates. Interestingly, the U32-A33 site located within the long stem region of HIV-RNA-1 was cleaved more efficiently than U51-A52 site, which was located within the opposite strand of the same stem region. This might be attributed to the variations in accessibility of these two regions and/or to the different levels of their structural tension, which may affect catalysis of transesterification of the RNA phosphodiester bonds. Indeed, our recent molecular dynamics simulations (Staroseletz, Nechaev et al., 2017) showed considerable changes in the fine structure of this stem regions. Electrophoretic mobility of fragments formed upon RNA

cleavage induced by the conjugates corresponded to the mobility of fragments formed by RNA cleavage with RNase T1 (Figure 2(A)) and 2 M imidazole buffer (primary data not shown), which suggests similar products formed upon cleavage with POCs and RNase T1. It is known that RNase T1 produces fragments bearing 5'-hydroxyl and 2',3'-cyclophosphate, similar to the RNA fragments that can be generated either through alkaline hydrolysis or in the presence of 2 M imidazole buffer. We can conclude therefore that the cleavage reaction catalyzed by **C1** and **C2** at physiological pH occurs through usual transesterification of the 2'-oxyanion onto the adjacent phosphorous atom leading to the formation of a di-anionic phosphorane intermediate, followed by the departure of the 5'-linked nucleoside and formation of a 2', 3' cyclic phosphate.

The hypothetical cleavage mechanism of RNA sequences by such peptidyl-oligonucleotide conjugates was discussed earlier (Lonnberg, 2011; Niittymaki & Lonnberg, 2006; Staroseletz, Williams et al., 2017; Williams et al., 2015), including the catalytic role of the guanidinium groups in promoting transesterification, as well as their synchronized action (Baldini et al., 2012; Salvio & Casnati 2017; Salvio et al., 2013; Staroseletz, Williams et al., 2017).

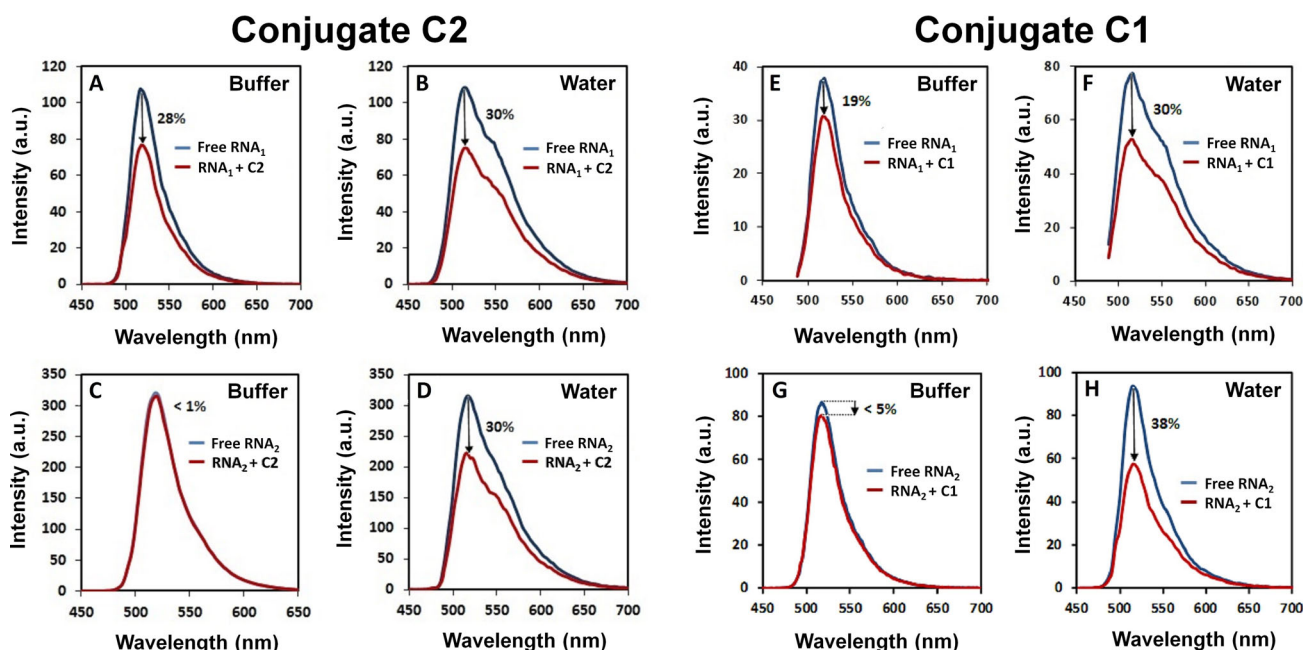


Figure 3. Fluorescence response on interaction of conjugate **C2** (left) or **C1** (right) with complementary (A–B and E–F, respectively) and non-complementary (C–D and G–H, respectively) RNA sequences in the presence and absence of mono-valent ions. Fluorescence emission spectra of the *complementary* target FAM-RNA₁ alone (blue) and after the addition of conjugate **C2** or **C1** (red) recorded in Tris-buffer (A and E, respectively) and in de-ionized water (B and F, respectively). Fluorescence emission spectra of the *non-complementary* RNA FAM-RNA₂ alone (blue) and after the addition of conjugate **C2** or **C1** (red) recorded in Tris-buffer (C and G, respectively) and in de-ionized water (D and H, respectively). The concentration of each component in the cuvette was 5 μ M. The spectra were recorded at 5 °C with the excitation wavelength set at 498 nm and 481 nm in Tris buffer and water, respectively. The slit width was 2.5 nm.

Remarkably, the base-specificity and the cleavage efficacy of this class of the peptidyl-oligonucleotide conjugates strongly depend on the nature, sequence and structural features of the RNA target. Earlier, **C1** and **C2** conjugates were evaluated against the linear (e.g. non-structured) *complementary* oligoribonucleotide 5'-[P³²]-GAUUGAAAUCCCC, which corresponded to a sequence from the anticodon arm of E.Coli tRNA^{Phe} (Pyshnyi et al., 1997, Mironova, Pyshnyi, & Ivanova, 2004) and had some sequence similarity with RNA₁ studied in this research. In contrast to the data presented here (see Figure 2(A)) showing clear Pyr-A preference in cleavage of 5'-[P³²]-RNA-HIV-1, both conjugates demonstrated exclusive G-X base-specificity for the site-directed cleavage of this short, linear complementary target, mainly at G1-A2 and G5-A6 positions. **C1** showed 80% cleavage activity, whereas the activity of **C2** against this target was not reported. Similarly, G-X base-specificity was detected again for these **C1** and **C2** conjugates, when they were studied against the linear (i.e. non-structured) *non-complementary* 20-mer sequence 5'-[P³²]-UUACACACACU GGAAGUUU (Mironova, Pyshnyi, & Ivanova, 2004), which had full homology with RNA₂ studied here. The overall cleavage efficiency of **C1** and **C2** against this target was found to be 80% and 63%, respectively, with the main cleavage sites seen at G12-G13, G13-G14, G14-A15 and G17-U18 positions (Mironova, Pyshnyi, & Ivanova, 2004). Neither peptide alone nor the mixture of the unconjugated peptide and oligonucleotide possessed cleavage activity, thus suggesting that only the hybrid *peptide-oligonucleotide* could promote catalysis.

3.3. 'Single-label' hybridization

Clear evidence of strong interactions at 1:1 molar ratio between the *complementary* RNA sequence and conjugate

C2 or **C1** (Figure 3), both in the presence of monovalent ions (i.e. in Tris buffer) and in their absence (i.e. in water), was provided by a noticeable response from fluorescein tag located at the 5'-terminal phosphate of the 2'-O-methyl-RNA sequences, which was also supported by UV-visible spectroscopy (see Figure S7 in the [Supplementary Material](#)). In Tris buffer, this can be attributed to the formation of the **C2:FAM-RNA₁** or **C1:FAM-RNA₁** duplexes stabilized by Watson-Crick hydrogen bonding between the oligonucleotide moiety of the POC and the complementary region of the RNA₁ sequence (see Figure 3(A,E), respectively). The oligonucleotide recognition component seemed to play the dominant role in the interactions between the **C2** or **C1** conjugates and the *complementary* target in the presence of a high level of counter cations under buffered-electrolyte conditions, which was sufficient to minimize repulsion between the negatively charged oligonucleotide strands, as demonstrated by a pictorial diagram shown in Figure 4.

However, in the absence of electrolyte, the peptide component seemed to become the key player in the interactions with both *complementary* and *non-complementary* target, when counter cations were insufficient or negligible in de-ionized water, thus allowing repulsion between the negatively-charged sugar-phosphate backbones of the oligonucleotides. Indeed, the addition of the conjugate **C2** or **C1** to the complementary target FAM-RNA₁ in water led to considerable quenching (30%) of the fluorescent signal in both cases (Figure 3(B,F), respectively). Thus, a high degree of binding to RNA through the peptide component was indicated when the strong electrostatic repulsion between the sugar-phosphate backbones of the oligonucleotides cannot be compensated by usual Watson-Crick hydrogen bonding between the complementary nucleotide residues.

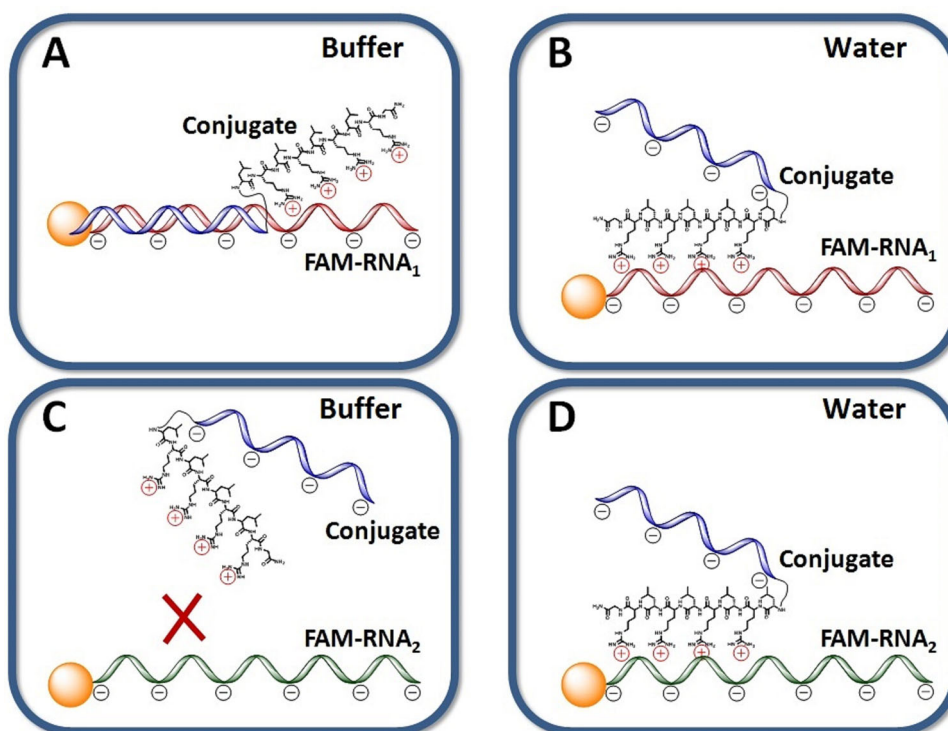


Figure 4. Pictorial diagram showing the predominant modes of interactions between the unlabeled conjugates **C1** or **C2** with complementary (A–B) and non-complementary (C–D) RNA sequences FAM-RNA₁ and FAM-RNA₂, respectively, in Tris buffer (A and C) or water (B and D). The orange spheres represent FAM fluorophore attached at the 5'-terminus of RNA₁ (red) or RNA₂ (green). The peptide component with four positively charged arginine residues is shown in black. Note that the position and orientation of the conjugate relative to the RNA strand in B and D could not be precisely defined and thus shown only schematically.

Similar levels of interaction were observed in water between these conjugates with the *non-complementary* target FAM-RNA₂, which was evident from considerable (30–38%) fluorescence quenching (Figure 3(D,H)), thus illustrating the predominance of nonspecific (in terms of RNA sequence) interactions in water, in the absence of physiological electrolyte.

Such interactions were also seen by UV-visible spectroscopy (see Figure S7 in the [Supplementary Material](#)). For example, conjugate **C2** interaction with the non-complementary FAM-RNA₂ target in water led to a 55% decrease in the intensity of the FAM absorption bands at around 360 - 510 nm (hypochromic effect). In addition, the absorption maxima λ_{\max} of this band was also blue shifted by 4 nm (to 454 nm) relative to the unbound FAM-RNA₂ target (458 nm). These observations were in agreement with the noticeable fluorescence response, thus confirming strong intermolecular interactions between **C2** and FAM-RNA₂ in water.

In the absence of the shielding effect from monovalent cations, the electrostatic interactions between the negatively-charged sugar-phosphate backbones of the RNA and the positively-charged arginine residues of the conjugates seem to become strong enough to prevent repulsion between the oligonucleotide moieties and stabilize nonselective *conjugate-RNA* complexes in de-ionized water. Under such conditions, the peptide seems to act as an 'electrostatic anchor' to hold all the components together (Figure 4(B,D) illustrates proposed arrangements).

The role of the electrostatic forces in these interactions was also evident from the fact that physiological concentrations (~200 mM) of monovalent counter cations, whether

predominantly Na⁺ (cf. extracellular) or K⁺ (cf. intracellular), completely suppressed the formation of any stable complexes between **C1** or **C2** conjugates and *non-complementary* RNA sequences (see Figure 3(C,G), respectively), presumably due to their competition for binding with the negatively-charged phosphate groups. Only negligible (<1%) or minor (<5%) fluorescence response was induced by addition of **C2** or **C1**, respectively, to FAM-RNA₂ in the Tris-buffered electrolyte (Figure 3(C,G), respectively). Moreover, we demonstrated by fluorescence recovery (see Figure S8 in the [Supplementary Material](#)) that the conjugates bound to the *non-complementary* RNA in water can be fully displaced from the complexes by simple injection of a high concentration of Na⁺ or K⁺ ions (up to 1 M). We conclude therefore that this interaction with *non-complementary* RNA was mediated mainly by the peptide moiety *via* electrostatic interactions with the RNA strand, which seems to represent the only possibility for interactions between the *non-complementary* RNA and the conjugates in water.

Our ¹H and ³¹P NMR studies of the *unconjugated* peptide with FAM-RNA₁ and FAM-RNA₂ (see Supplementary Figures S9–S14) provided additional evidence of the predominant role of the electrostatic forces in their interactions. Relatively sharp ¹H or ³¹P NMR signals of FAM-RNA₁, typical for unbound molecular species, showed marked line broadening upon mixing of these two components together in water (Supplementary Figures S9 and S10, respectively). This was accompanied by a decrease of signal intensities, presumably due to formation of multiple conformational species of the *peptide-RNA* complexes formed. In addition, some peptide ¹H signals showed noticeable (0.04 - 0.08 ppm) up-field shifts upon interaction with RNA. However, the addition of NaCl in

excess (1 M final concentration) reversed signal broadening and led to substantial or full recovery of their intensities and chemical shifts. When FAM-RNA₁ (30 μM) was initially pre-mixed with NaCl (250 mM), the subsequent addition of the 4-fold excess of peptide (to achieve 120 μM) had no significant effect on ³¹P NMR spectra of RNA (see [Supplementary Figure 11](#)) and led to only very minor changes in positions of some ¹H NMR peaks of FAM-RNA₁ (see [Supplementary Figure 12](#)). This was presumably due to the presence of the high concentration of counter cations in the sample, which blocked any potential *arginine-phosphate* nonspecific electrostatic interactions. Similar effect was observed for the non-complementary FAM-RNA₂ upon addition of the unconjugated peptide in Tris-buffered electrolyte (50 mM Tris-HCl, pH 7.0, 200 mM KCl and 0.5 mM EDTA). ¹H NMR and ³¹P NMR spectra recorded for individual FAM-RNA₂ and peptide components showed no significant differences after mixing them together, thus eliminating any possibility of stable complex formation between these components in the presence of counter cations at sufficient concentrations (see [Supplementary Figures 13 and 14](#), respectively).

Nevertheless, the contributions of some other molecular forces (e.g. hydrogen bonding between guanidinium groups of arginine and guanosine residues) cannot be fully excluded from the factors stabilizing *RNA-peptide* or *RNA-conjugate* interactions. Indeed, it was recently reported (Krishna et al., 2019) that a guanidinium moiety, when incorporated into the middle of the PNA chain, could serve as a hydrogen bond donor and potentially form two hydrogen bonds with the guanosine residue of the G-C base-pair within the *double-stranded* RNA target, provided that these interactions were additionally stabilized through triplex formation by the PNA nucleotides flanking such guanidinium groups. However, this cannot be assumed for single-stranded RNA sequences, because hydrogen bonds between guanidinium groups and *unpaired* guanosine residues appeared to be unstable. In fact, the binding affinity of the PNA incorporating guanidinium moiety toward *single-stranded* RNA (relevant to this study) was shown to be 14 times lower than that toward *double-stranded* RNA (Krishna et al., 2019). These results seemed to agree with our molecular modeling simulations, which demonstrated the possibility of hydrogen bonding interactions between the arginine side-chain with the N₇ and carbonyl O atoms of guanosine residues (Patutina et al., 2017). However, these interactions appeared to be ancillary, whereas the network of ionic interactions between arginine residues with backbone phosphate groups of RNA was shown to dominate such interactions.

The predominant modes of interactions indicated by these studies between the unlabeled conjugates **C1** and **C2** with the complementary and non-complementary RNA targets FAM-RNA₁ and FAM-RNA₂, respectively, are depicted in [Figure 4](#), for the two experimental extremes of buffered electrolyte (A and C) and de-ionized water (B and D).

3.4. 'Dual label' hybridization

Dually-labelled systems (see [Figure 1\(C,D\)](#)) with two fluorescent tags, one attached to the 3'-terminus of the conjugate

C3 (i.e. 3'-Cy3) and the other attached to the 5'-terminus of the RNA target (i.e. 5'-FAM) provided insight into the relative location of individual components and illuminated their particular roles in binding events, both in water and buffered electrolyte.

The overall response on binding was more pronounced ([Figure 5](#)) for the dually-labelled systems, but demonstrated very similar behavior patterns to those observed earlier for the unlabeled **C1** or **C2** conjugates. Indeed, the hybridization of the FAM-RNA₁ with **C3** in Tris-buffered electrolyte led to an 87% decrease of the fluorescence in both cases: when the hybridization event was monitored by following the emission of FAM-RNA₁ (excited at 496 nm) upon the addition of **C3** ([Figure 5\(A\)](#)); and, in the parallel studies, by looking at the emission of Cy3-labelled conjugate ([Figure 5\(B\)](#)) upon the addition of FAM-RNA₁ (excited at 552 nm). In each case, this considerable quenching of fluorescence was accompanied by a small, but reproducible (1–2 nm) shift in the emission λ_{max} to a longer wavelength (bathochromic shift) seen for either FAM or Cy3 emission band.

Both the nature and the scale of these reciprocal responses from the two fluorophores within the dually-labelled system were somewhat unexpected. FAM and Cy3 have been often used in as a *Donor-Acceptor* couple in FRET, due to the substantial overlap of the emission spectrum of FAM with the excitation spectrum of Cy3 (Chen et al., 2010; Olejko et al., 2016; Olejko & Bald, 2017; Tsourkas et al., 2003; Zhao et al., 2010). In the case of Förster resonance energy transfer from FAM (acting as a *Donor*) to Cy3 (acting as an *Acceptor*), the observed decrease of FAM fluorescence is usually coupled with an increase of Cy3 fluorescence. Instead here with dually-labelled components, we detected very strong quenching of *both* emission bands triggered by their self-assembly. A possible explanation of such mutual quenching of the fluorophores could be a formation of a non-fluorescent complex between the excited fluorophore (FAM) and another fluorophore molecule (Cy3) *via* 'contact quenching' (also known as a 'static quenching') (Crisalli & Kool, 2011; Johansson et al., 2002; Marras et al., 2002).

In 'contact quenching', the donor and acceptor molecules interact *via* a proton-coupled electron transfer through the formation of hydrogen bonds at their ground-state, which are often controlled by electrostatic and/or hydrophobic forces. When such a ground-state hetero-dimer is excited using a resonant electromagnetic radiation wavelength, the resulting excited state immediately returns to the ground state without emission of a photon. As a result, such ground-state complex does not emit fluorescence upon excitation. A characteristic feature of such 'contact quenching' is a change in the UV-visible absorption spectrum of this ground-state complex, as compared to that of the individual components (Crisalli & Kool, 2011; Johansson et al., 2002; Marras et al., 2002). This is different from the FRET mechanism, when UV-visible absorbance of the complex is expected to be an additive of the spectral contributions of the individual molecules. Also, FRET does not require very close proximity of two fluorophores and may occur over relatively long distances from 10 to 100 Å, which is approximately the distance between 3

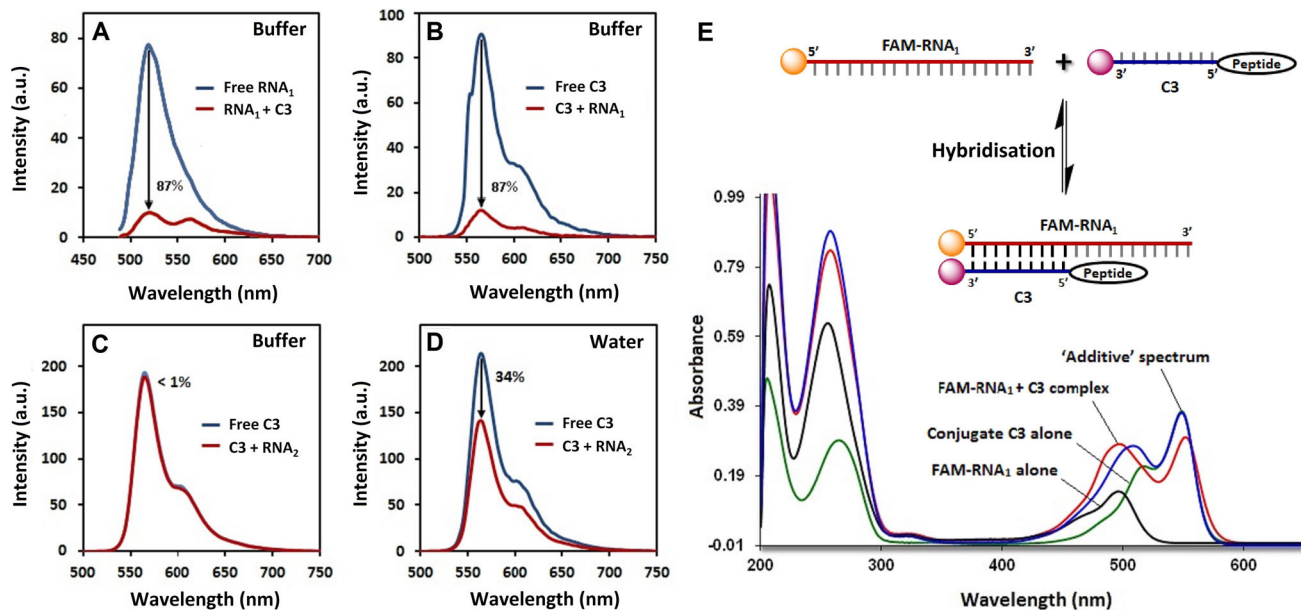


Figure 5. (A–B) Fluorescence response on interaction of **C3** with *complementary* target FAM-RNA₁ in Tris buffer. (A) Fluorescence spectra of FAM-RNA₁ alone (blue) and after the addition of conjugate **C3** (red). (B) Fluorescence spectra of the Cy3-labeled conjugate **C3** alone (blue) and after the addition of FAM-RNA₁ target (red). (C–D) Fluorescence response on interaction of **C3** with *non-complementary* target FAM-RNA₂ in Tris buffer (C) and water (D). Fluorescence spectra of the Cy3-labeled conjugate **C3** alone (blue) and after the addition of FAM-RNA₂ sequence (red). The spectra were recorded following excitation either of FAM at 496 nm (A) or Cy3 at 552 nm (B–D). The concentration of each component in the test cuvette was 2.5 μ M, and slit width of 2.5 nm was used for both excitation and emission. Emission maxima at around 520 nm and 560 nm correspond to the fluorescence bands of FAM and Cy3, respectively. (E) UV-visible spectra of the unbound FAM-RNA₁ (black), free conjugate **C3** (green) and their mixture (red). Blue curve shows the ‘additive’ spectrum obtained by summing of the absorption spectra of the FAM-RNA₁ and **C3**. All spectra were recorded under identical conditions in Tris buffer at 5 °C. The concentrations of the components in the test cuvette were 2.5 μ M.

and 30 nucleotides in a double-stranded DNA molecule (Bichenkova et al., 2011; Marras et al., 2006).

In order to investigate whether Cy3 and FAM fluorophores form such a ground-state complex upon hybridization of **C3** with the complementary target FAM-RNA₁, we recorded the separate UV-visible spectra of the free conjugate **C3**, unbound FAM-RNA₁, as well as their equimolar mixture in Tris-buffered electrolyte (Figure 5(E)). The UV-visible spectrum of the **C3**:FAM-RNA₁ complex (red) cannot be reconstructed by summing the absorption spectra of the free **C3** (green) and unbound FAM-RNA₁ (black), and thus is not merely additive (cf. red and blue curves in Figure 5(E), where blue curve corresponds to the ‘additive’ spectrum obtained by summing of the absorption spectra of the FAM-RNA₁ and **C3**). These observations suggest a certain degree of intermolecular interactions between Cy3 and FAM at their ground state, which led to the formation of a hetero-dimer between two fluorophores with its own, distinctive electronic properties, such as being non-fluorescent and having unique UV-visible characteristics. Therefore, this significant, mutual quenching in fluorescence seen for both fluorophores on hybridization in buffer conditions (Figure 5(A,B)) is likely to be attributed to ‘contact quenching’, indicative of a very close location of FAM and Cy3 within the **C3**:FAM-RNA₁ complex in buffered electrolyte, such as to allow for direct proton-coupled electron transfer at their ground states. This hypothesis is consistent with the earlier proposed model of the interaction between the conjugate and complementary RNA target in the presence of counter cations (see Figure 4(A)). A pictorial diagram showing possible mode of interactions between the Cy3-labelled conjugate **C3** and the complementary target FAM-RNA₁ in Tris-buffered electrolyte is given in Figure 6(A), that emphasizes the key role of the oligonucleotide component

in the presence of a high level of counter cations, which are necessary to prevent repulsion between the negatively-charged complementary oligonucleotide strands.

In contrast, the conjugate **C3** showed negligible interactions with the *non-complementary* RNA sequence under identical conditions (i.e. Tris buffer in Figure 5(C)). Presumably, the presence of excess counter cations effectively suppressed any possible electrostatic interaction between the conjugate and the non-complementary RNA target, where sequence-specific Watson-Crick hydrogen bonds could not be formed between the non-complementary oligonucleotide sequences (Figure 6(C)).

The mode of interaction of the conjugate **C3** toward both complementary (FAM-RNA₁) and non-complementary (FAM-RNA₂) RNA seemed to completely change in water, in the absence of electrolyte. Indeed, the level of Cy3 fluorescence quenching on binding with RNA dropped from 87% in buffer (Figure 5(A,B)) to only 8% for the **C3**:FAM-RNA₁ complex in water (Table 1), which presumably indicates the higher degree of separation between Cy3 and FAM under these conditions. The interaction between the non-complementary target FAM-RNA₂ and the **C3** conjugate in water also showed the reduced level of response (34% fluorescence decrease) from the Cy3 tag (Figure 5(D)). This behavior corresponds well with the model proposed earlier for **C2** and **C1** in water (Figure 4(B,D)), when the detected interactions with RNA are mediated mainly by the peptide component *via* electrostatic interactions, so that RNA and the oligonucleotide component become rather distant (Figure 6(B,D)). According to this model, separation between the FAM and Cy3 within the **C3**:FAM-RNA₁ complex becomes significant, thus reducing or eliminating completely the contribution from the ‘contact quenching’ for these two fluorophores.

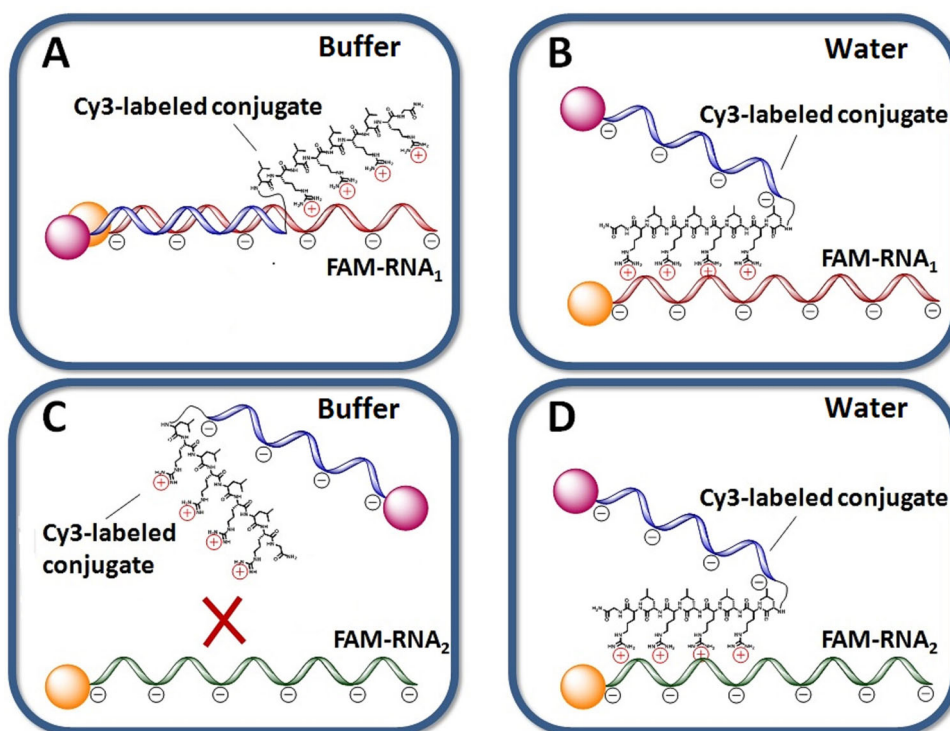


Figure 6. Pictorial diagram showing the predominant modes of interactions of the Cy3-labeled conjugate C3 with complementary (A–B) or non-complementary (C–D) RNA sequences FAM-RNA₁ or FAM-RNA₂, respectively, in buffer or in water. The orange spheres represent FAM fluorophore attached at the 5'-terminus of RNA₁ (red) or RNA₂ (green), whereas the pink spheres show Cy3 dye attached at the 3'-position of the conjugate C3. The peptide component with four positively charged arginine residues is shown in black. Note that the position and orientation of the conjugate relative to the RNA strand in B and D could not be precisely defined and thus shown only schematically.

3.5. Melting temperature profiles

Additional evidence in support of our hypothesized interactions between the conjugates **C1**, **C2** and **C3** with the complementary target RNA₁ in buffered electrolyte and water was provided by melting temperature measurements (Figure 7(A–I)). As expected, the T_m profile of the complex formed between conjugate **C2** and FAM-RNA₁ (Figure 7(A)) revealed a sigmoidal curve, typical for double-stranded nucleic acids, with T_m value of 29 °C and 23% hyperchromicity. This characteristic temperature-induced transition seems to be attributed to the dissociation of the duplex formed by the conjugate and its complementary RNA target. Although the melting curve obtained for the **C1**: FAM-RNA₁ complex in buffered electrolyte (Figure 7(B)) was not very well defined, due to a lower stability of the shorter duplex formed between the 6-mer conjugate **C1** and the complementary region of the FAM-RNA₁, there was a clear indication of sigmoidal-like transition with the T_m around 17 °C and 15.5% hyperchromicity. It was not possible to obtain a low-temperature plateau for this short complex, as this region was below 0 °C. However, this data indicated that at 5 °C **C1** and FAM-RNA₁ seem to exist predominantly in a duplex form, which is in agreement with the fluorescence data. The peptide seemed to stabilize complexes formed between conjugates and RNA, presumably by nonspecific electrostatic interactions. This was supported by the slight increase in T_m value seen for the **C2**:FAM-RNA₁ as compared to that of the 'control' duplex **ON**₂-FAM-RNA₁ (T_m =24 °C) (cf. Figure 7(A and E)).

Interestingly, the melting temperature profiles observed in water for the **C2** and **C1** conjugates with both the complementary FAM-RNA₁ target (Figure 7(C,D), respectively) as well as with non-complementary FAM-RNA₂ target (Figure 7(G,H), respectively) revealed a co-operative, sigmoidal-like transition, which is more typical for thermal denaturation of a double-stranded duplex, although the temperature intervals for the transitions in water were in general considerably broader than those seen in buffered electrolyte. The observed S-like character of the melting curves seen for the **C2**:FAM-RNA₁, **C2**:FAM-RNA₂, **C1**:FAM-RNA₁ and **C1**:FAM-RNA₂ complexes in water suggests an involvement of numerous nonspecific contacts between adjacent nucleotides and amino acid fragments, which thereby showed cooperative behavior. The higher thermal stability of the **C1**:FAM-RNA₂ and **C1**:FAM-RNA₁ complexes in water (T_m =30 °C and T_m =33 °C, respectively) than those seen for the **C2**:FAM-RNA₂ and **C2**:FAM-RNA₁ (T_m =24 °C and T_m =27 °C, respectively) under identical conditions correlates well with the smaller net-negative charge of the conjugate **C1** (i.e. –2), as compared to that seen for the conjugate **C2** (i.e. –5), and the corresponding reduction of repulsive forces with the negatively-charged FAM-RNA₁ or FAM-RNA₂. The lower level of hyperchromicity of these transitions (cf. 16.5% and 20.9% hyperchromicity for **C2**:FAM-RNA₂ and **C2**:FAM-RNA₁, respectively, in water against 23% hyperchromicity for **C2**:FAM-RNA₁ in Tris-buffered electrolyte) probably indicates that the degree of π - π stacking interactions within the **C2**:FAM-RNA₂ and **C2**:FAM-RNA₁ complexes formed in water is

Table 1. Summary of hybridization monitored by fluorescence and T_m profiles for six studied systems, **C1:FAM-RNA₁**, **C1:FAM-RNA₂**, **C2:FAM-RNA₁**, **C2:FAM-RNA₂**, **C3:FAM-RNA₁** and **C3:FAM-RNA₂**. Experiments were carried out in Tris buffer (50 mM Tris, 200 mM KCl, 0.5 mM EDTA, pH 7.0) or in water at 5 °C.

| Conjugate-RNA system | Relative change of fluorescence intensity on hybridization (%) ^a | | T_m (°C) (Hyperchromicity, %) ^b | |
|-------------------------------|-----------------------------------------------------------------------------|-------|----------------------------------------------|-----------|
| | Buffer | Water | Buffer | Water |
| C2:FAM-RNA₁ | 28 | 30 | 29 (23) | 27 (20.8) |
| C2:FAM-RNA₂ | <1 | 30 | ND | 24 (16.5) |
| C1:FAM-RNA₁ | 19 | 30 | 17 (15.5) | 33 (20.9) |
| C1:FAM-RNA₂ | <5 | 38 | ND | 30 (15) |
| C3:FAM-RNA₁ | 87% | 8 | 33 (20) | ND |
| C3:FAM-RNA₂ | <1 | 34 | ND | 27(15) |

^aRelative change of fluorescence intensity on hybridization between RNA and conjugate was calculated as $\frac{F(RNA) - F(Complex)}{F(RNA)} \times 100\%$, where $F(RNA)$ refers to the fluorescence intensity of the test cuvette containing the target sequence alone (i.e. FAM-RNA₁ or FAM-RNA₂) and $F(Complex)$ refers to the fluorescence intensity of the test cuvette after the addition of the conjugate. Experimental errors in estimation of relative change of fluorescence intensity on hybridization usually ranged between 1.4 and 2%.

^b T_m (°C; in bold) refers to the melting temperature (°C) of the hybridized complex, measured from the UV-monitored melting temperature profiles at 260 nm. Figures in brackets (in italics) represent the level of hyperchromicity (%) measured from T_m profile. ND – Not detectable due to absence of sigmoidal T_m profile.

Table 2. Through-space ¹H-¹H NOE interactions detected from *inter-nucleotide* and *peptide-nucleotide* interactions, as well as from *intra-* and *inter-peptide* interactions observed in the ¹H NOESY spectrum (Figure 8) of the conjugate **C2**.

| Selected ¹ H NOESY interactions | | | |
|-----------------------------------------------------------|---------------------------------------------|----------------------------------------------------------------------------|------------------------------------------------------------------------------|
| Inter-nucleotide | Peptide – oligonucleotide | | Inter-peptide |
| | Arginine – nucleotide | Leucine – nucleotide | |
| a: ⁸ T 5(CH ₃) – ⁷ A H8 | h: Arg 5-HH – ¹⁻³ T H1' | k: ¹ Leu 2-H – ¹ T H1' | r: ¹ Leu 3-HH – Arg 5-HH |
| b: ⁸ T 5(CH ₃) – ⁹ C H6 | i: Arg 5-HH – ¹⁻³ T H4'/H5'/H5'' | l: ¹ Leu 5-(CH ₃) ₂ – ¹ T H6 | s: ¹ Leu 5-(CH ₃) ₂ – Arg 5-HH |
| c: ⁸ T H6 – ⁹ C H6 | j: Arg 5-HH – ¹⁻³ T H6 | m: ¹ Leu 3-HH – ¹ T H6 | t: ¹ Leu 5-(CH ₃) ₂ – ¹ Leu 2-H |
| d: ⁴ T H6 – ⁵ C H6 | | n: ¹ Leu 3-HH – ¹ T H1' | u: ¹ Leu 3-HH – ¹ Leu 2-H |
| e: ⁴ T H6 – ⁵ C H5 | | o: ¹ Leu 5-(CH ₃) ₂ – ¹ T H1' | v: ¹ Leu 2-H – Arg 5-HH |
| f: ⁷ A H8 – ⁶ A H8 | | p: ¹ Leu 2-H – ¹ T H4'/H5' /H5' | |
| g: ⁸ T H6 – ⁷ A H8 | | q: ¹ Leu 2-H – ¹ T H6 | |

considerably lower than that within the regular, double-stranded duplex (e.g. **C2:FAM-RNA₁** in buffered electrolyte), formed by the fully-complementary oligonucleotides.

The dually-labelled **C3:FAM-RNA₁** formed between the Cy3-labelled conjugate **C3** and the complementary RNA target showed a 4 °C increase in T_m value in buffered electrolyte, as compared with its unlabeled counterpart, **C2:FAM-RNA₁** (cf. Figure 7(F) and Figure 7(A)), presumably due to extra molecular interactions (i.e. between the Cy3 and FAM dyes). This observation supports the proposed earlier hypothesis on the formation of the ground-state complex between the closely located fluorophores upon hybridization of **C3** with the complementary target FAM-RNA₁ (Figure 6(A)), which led to a considerable decrease of the fluorescence (Figure 5(A,B)), presumably, due to 'contact quenching', and to a change in the UV-visible spectrum (Figure 5(E)) for **C3:FAM-RNA₁** complex in buffered electrolyte. The melting temperature profiles of the **C3:FAM-RNA₂** complex between the Cy3-labelled conjugate **C3** and the non-complementary RNA target in water (Figure 7(I)) showed T_m value of 27 °C. Again, the dually-labelled system **C3:FAM-RNA₂** showed a small, but reproducible increase in T_m in water, as compared with its mono-labelled counterpart, **C2:FAM-RNA₂** (cf. Figure 7(I) and Figure 7(G)). For convenience, Table 1 summaries the hybridization studies monitored by fluorescence and T_m profiles for the six studied systems, **C1:FAM-RNA₁**, **C1:FAM-RNA₂**, **C2:FAM-RNA₁**, **C2:FAM-RNA₂**, **C3:FAM-RNA₁** and **C3:FAM-RNA₂**.

We also recorded T_m profiles for the free conjugates **C1** and **C2**, as well as for the isolated FAM-RNA₁ and FAM-RNA₂ in the absence or presence of the peptide, which were measured either in water or in Tris buffer (see Supplementary

Figure S15). In contrast to the co-operative behavior of the **C1:FAM-RNA₁**, **C1:FAM-RNA₂**, **C2:FAM-RNA₁** and **C2:FAM-RNA₂** complexes during their thermal denaturation (see Figure 7), the isolated components **C1**, **C2**, FAM-RNA₁ and FAM-RNA₂ did not show the sigmoidal character of their T_m profiles, thus indicating the absence of any folding or stable secondary structures. The only slight exception was seen for FAM-RNA₁ in Tris buffer, which showed a minor *low-temperature* transition at 5 °C–15 °C interval with mild (6.7%) hyperchromicity, which could signify the presence of short, unstable duplex-like regions. In Tris buffer, the addition of the unconjugated peptide to RNA₁ or RNA₂ had no effect on the shape of the T_m profiles (see Supplementary Figure S15, C and E), thus confirming the absence of any stable *RNA-peptide* interactions in the presence of counter cations at sufficient concentrations. However, we could not fully exclude such possibilities when these experiments were carried out in de-ionized water (Supplementary Figure S15, D and F), although the impact of the peptide on the shape of the RNA T_m profiles was only minor and not well-defined.

3.6. NMR evidence of conjugate folded structure

The ability of the positively-charged amphipathic peptide to interact with the negatively-charged sugar-phosphate backbone of nucleic acids in the absence of counter cations, demonstrated in this research, suggested the high probability of strong *intra-molecular* interactions between the peptide and oligonucleotide components within the same conjugate molecule. In order to investigate this possibility, we recorded a ¹H-NOESY spectrum (500 MHz) of **C2** in D₂O

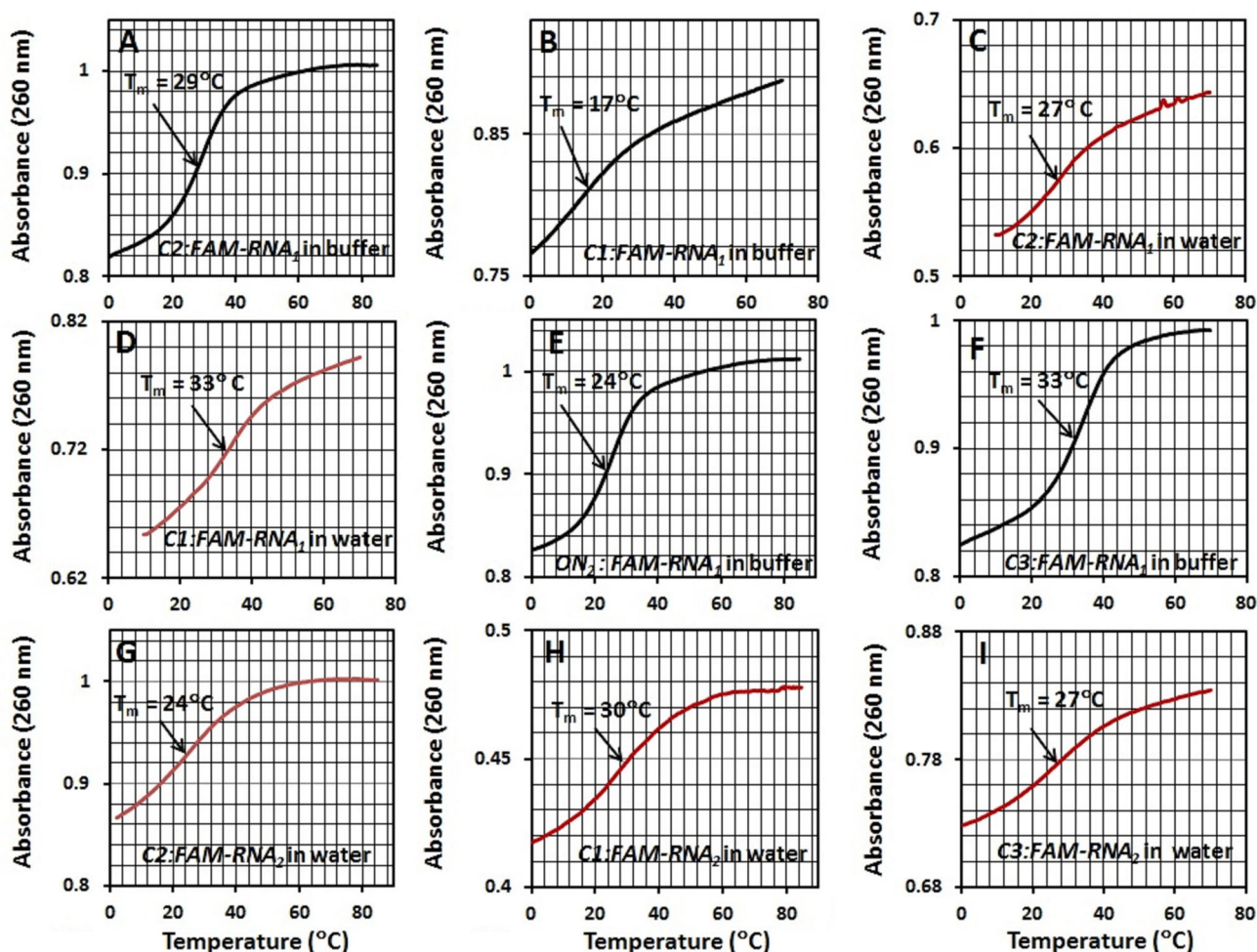


Figure 7. T_m profiles of the complexes formed by conjugates **C2**, **C1** and Cy3-labelled conjugate **C3** with complementary ($FAM-RNA_1$) and non-complementary ($FAM-RNA_2$) targets, measured at 260 nm. (A, B and F) T_m profiles (black) of the $C2:FAM-RNA_1$, $C1:FAM-RNA_1$ and $C3:FAM-RNA_1$ complexes, respectively, recorded in Tris buffer. (C, D, G, H and I) T_m profiles (red) of the $C2:FAM-RNA_1$, $C1:FAM-RNA_1$, $C2:FAM-RNA_2$, $C1:FAM-RNA_2$ and $C3:FAM-RNA_2$ complexes recorded in de-ionized water. (E) T_m profile (black) of the 'control' $ON_2:FAM-RNA_1$ duplex in Tris buffer. The concentration of each component in the cuvette was 2.5 μM . The temperature gradient was 0.1 $^{\circ}C/min$, and the data collection interval was 0.1 $^{\circ}C$. T_m values were calculated by the first derivative method.

(Figure 8) with the aim to assess: (i) whether these conjugates can adopt any stable, predominant conformation; and (ii) whether the peptide and oligonucleotide elements form any detectable interactions within the conjugate structure.

The full 1H -NOESY NMR spectrum of **C2** conjugate (Figure 8(A)) showed NOE cross-peaks arising from *intra*- and *inter*-nucleotide interactions, *intra*- and *inter*-peptide interactions, as well as *peptide-nucleotide* interactions, which can only be detected between nuclei separated by less than 5 angstroms. Full signal assignment of the oligonucleotide protons was achieved through well-established NOE connectivity:

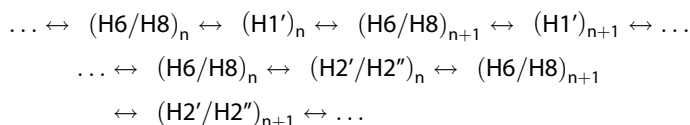


Figure 8(B) presents the extended part of the NOESY spectrum showing the $H6/H8 \leftrightarrow H1'/H5$ region as an example. Generally, the 1H NOESY spectra of the conjugate **C2** (Figure 8) signify the presence of a dominant rigid structure within the conjugate in water (D_2O). The observed NOE-interactions, which are rather unusual for single-stranded DNA, suggest that the oligonucleotide part of

the conjugate has a substantial population of the pre-organized helical structure. Furthermore, the inter-residue *peptide-peptide* NOE interactions detected between Arg-5HH and Leu-3HH, Leu-4H and Leu-5(CH_3) protons (Figure 8) are in line with the previous reports on circular dichroism studies of this class of conjugates (Mironova et al., 2006), which have shown the alteration of the peptide structure upon conjugation to oligonucleotides.

Strong NOE interactions were observed between the first two amino acid residues (1Leu and 2Arg) and the first three thymidine nucleotide residues (1T , 2T and/or 3T) of the conjugate **C2**. Unfortunately, due to the repetitive nature the oligonucleotide part of the conjugate (H_2N -Gly-[Arg-Leu] $_4$ - $p^{1-3}T^{2-4}T^{5-6}A^{7-8}T^{9-3}$), the first three thymidine residues produce strongly coinciding 1H signals, leading to overlapping $^1Arg/^2Leu$ - ^{1-3}T NOESY cross-peaks, which were difficult to distinguish. However, the spectra displayed a number of crucial cross-peaks between arginine 5-HH protons and H6 and sugar ring protons of 1T , 2T and/or 3T (indicated by green circles), which include: Arg 5-HH ^{1-3}T H6, Arg 5-HH \leftrightarrow ^{1-3}T H1' and Arg 5-HH \leftrightarrow ^{1-3}T H4'/H5'/H5'' (Figure 8(A)).

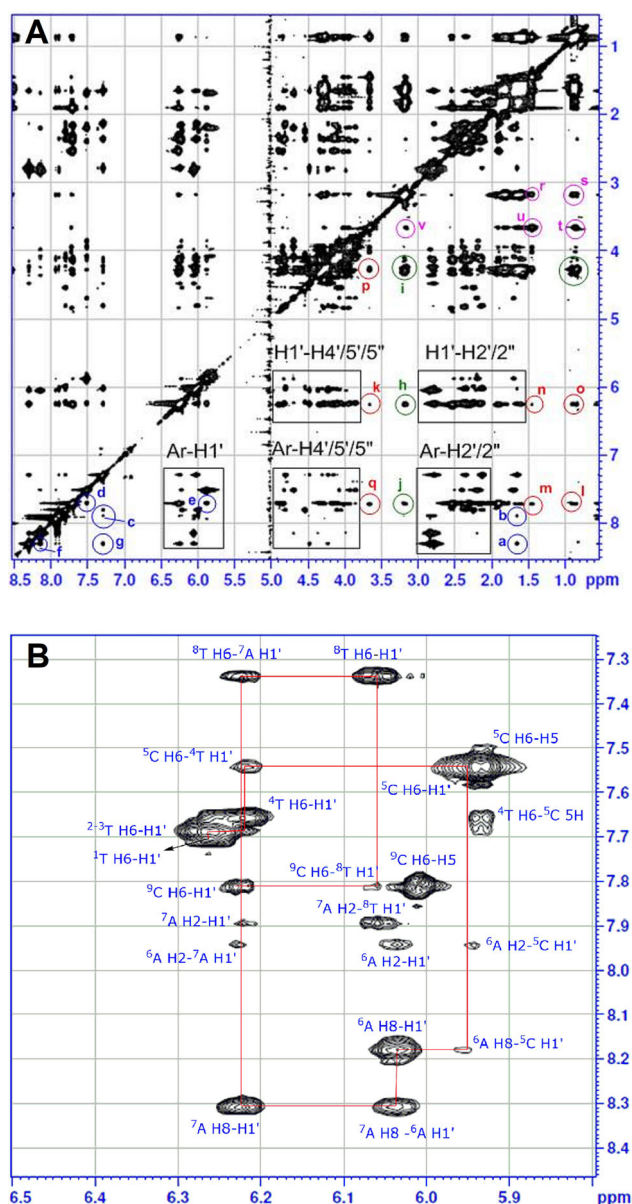


Figure 8. 2D ^1H NOESY NMR spectra of the conjugate **C2** recorded in D_2O at 25°C (500 MHz, Bruker AVANCE II+, 2.5 mM, 0.5 s mixing time). (A) Full ^1H NOESY spectrum showing the key oligonucleotide and peptide proton resonance regions. Some important ^1H - ^1H NOE cross-peaks arising from *inter*-nucleotide and *peptide-nucleotide* interactions, as well as from *intra*- and *inter*-peptide interactions of the conjugate are labelled by symbols (a)–(v) and summarized in Table 2. Nomenclature and numbering of hydrogen atoms used for assignment of the peptide and oligonucleotide ^1H NMR signals is shown in Figure S1 and Figure S2, respectively (see Supplementary Material). (B) Expanded region of the ^1H NOESY spectrum of the conjugate $\text{H}_2\text{N-Gly-}[\text{Arg-Leu}]_4\text{-}^5\text{p}^1\text{T}^2\text{T}^3\text{T}^4\text{T}^5\text{C}^6\text{-A}^7\text{A}^8\text{T}^9\text{C}^3\text{'}$ (D_2O , 5°C , 500 MHz, 2.5 mM, 0.5 s mixing time), showing NOE interactions between the aromatic (H6/H8) and the H1' protons of the oligonucleotide part of the conjugate **C2**. The route for sequential assignment was based on the ^1H NOE connectivity: $\leftrightarrow (\text{H6/H8})_n \leftrightarrow (\text{H1}')_n \leftrightarrow (\text{H6/H8})_{n+1} \leftrightarrow (\text{H1}')_{n+1}$, which is indicated by a red line in the spectrum. This network shows through-space contacts between the H1' sugar ring protons of the residue n with its own aromatic H6/H8 protons as well as with the H6/H8 protons of the next $(n+1)$ residue. Cytidine H5-H6 interactions for the ^5C and ^9C residues are also indicated.

The NOESY spectrum of **C2** also displayed several other NOE interactions between ^1Leu and ^{1-3}T residues of the conjugate. These include: ^1Leu 2-H ^{-1}T H1', ^1Leu 5-(CH_3) $_2$ ^{-1}T H6, ^1Leu 3-HH ^{-1}T H6, ^1Leu 3-HH ^{-1}T H1', ^1Leu 5-(CH_3) $_2$ ^{-1}T H1', ^1Leu 2-H ^{-1}T H4'/H5'/H5'' and ^1Leu 2-H ^{-1}T H6 (red colored cross-peaks). These NOESY interactions indicate close contacts between the first two amino acid residues of the catalytic peptide and the first 3 nucleotide residues (^1T , ^2T and/or ^3T) of the oligonucleotide, indicating the predominance of a stable, folded conformation of the conjugate in water with a structural U-turn between Leu^1 and ^1T residues, as shown in the Supplementary Figure S16.

In summary, we provide NMR evidence of a stable, hair-pin-like folded conformation of the conjugates, which seems to dominate in water and can be stabilized by π - π stacking interactions between nucleotide aromatic bases, as well as by *inter*-residue contacts between oligonucleotide and peptide fragments.

3.7. Dimer formation

The amphipathic nature of the peptide component within POCs, and the fact that each conjugate contains both positively-charged (i.e. peptide) and negatively-charged (i.e.

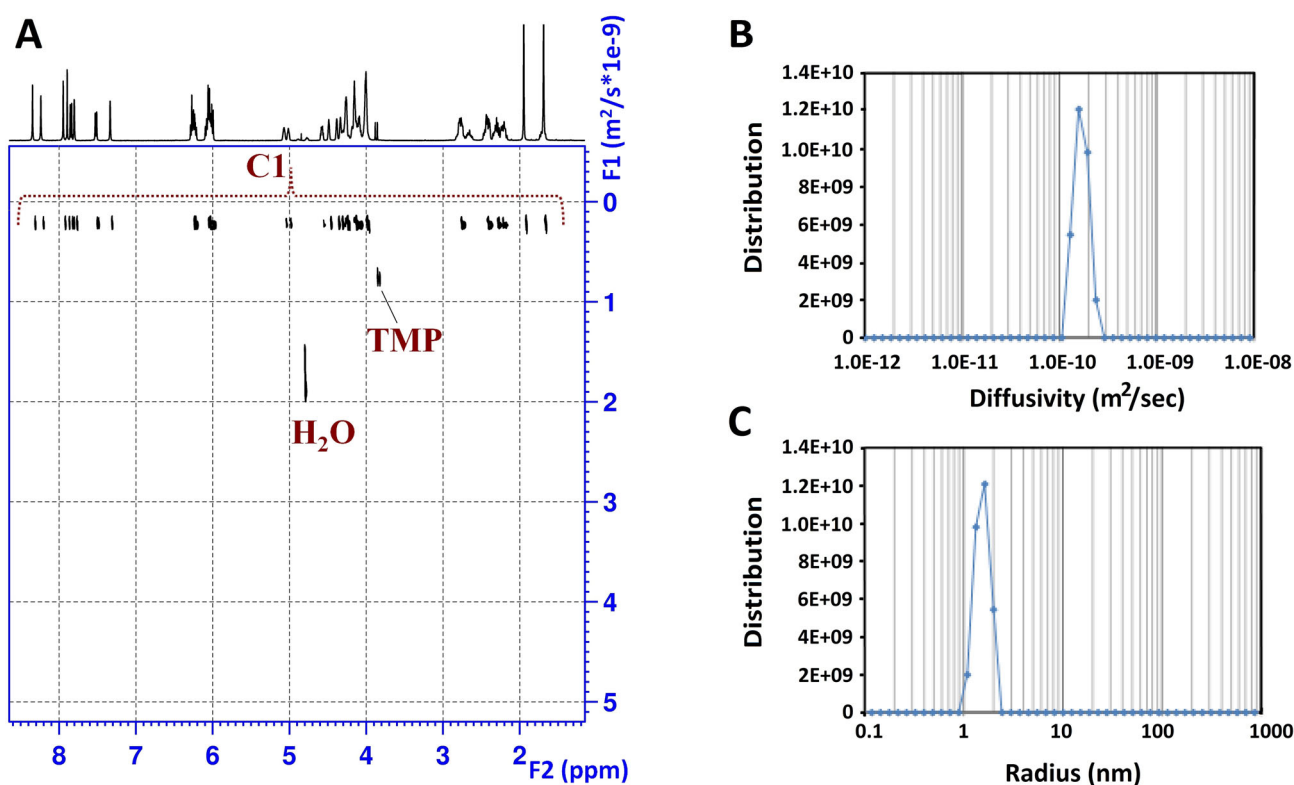


Figure 9. (A) Pseudo 2D representation of C1 diffusion at room temperature (produced using Bruker TopSpin® 2.0 software). (B) Diffusion coefficient plot for C1 conjugate. (C) Size distribution for C1 molecular species in the NMR sample obtained after inversion with CONTIN.

oligonucleotide) components, suggested that they may potentially form *inter*-molecular assemblies. We investigated this possibility by analysis of changes in hydrodynamic radius of one of the conjugates (**C1**) by measuring its molecular diffusion in aqueous solution using Diffusion Ordered Spectroscopy (Figure 9). The diffusion constant D of a molecule can be correlated to its shape and size by the Stokes-Einstein equation (Valentini et al., 2004):

$$D = \frac{kT}{6\pi\eta r_s}$$

where D is the diffusion coefficient, k is Boltzmann constant, T is the temperature, η is the viscosity of the solution and r_s is the hydrodynamic radius of the particle.

The diffusion coefficient D of the conjugate was measured by ^1H DOSY (Bichenkova et al., 2017; Provencher, 1982a, 1982b; Valentini et al., 2004) from the ratio between the intensity of the attenuated NMR signal I and the initial signal I_0 (as described in the 'Material & Methods' section) using the Stejskal-Tanner equation (Kersebaum & Salnikov, 2006):

$$\frac{I}{I_0} = e^{-D\gamma^2 g^2 \delta^2 (\Delta - \frac{\delta}{2})}$$

where D is the diffusion coefficient, γ is the gyromagnetic ratio, g is the gradient field pulse strength, δ is the gradient field pulse length and Δ is the diffusion time.

The diffusion coefficients of various molecular species, which often exist in a fast exchange within the complex sample, may have close values that are difficult to resolve due to a continuous distribution of particle sizes. To mitigate this

matter, we used an inverse Laplace transform (also known as CONTIN algorithm) (Provencher, 1982a; Valentini et al., 2004) in an attempt to provide the distribution of the diffusion coefficients for **C1** and, if possible, to resolve the individual diffusion coefficients in the mixture of different molecular species with close diffusion coefficients. **C1** conjugate molecules were present in solution with diffusion coefficients ranging between 2.37×10^{-10} and $1.29 \times 10^{-10} \text{ m}^2/\text{s}$ (Figure 9), suggesting predominant molecular species with close molecular radii ranging from 1.0 nm to 2.0 nm, which corresponds to particle diameters ranging from 20 Å to 40 Å.

The estimated overall length of the folded structure of the **C1** conjugate, evaluated using molecular graphics ranged between 21 Å and 23 Å, which shows reasonable agreement with the lowest size limit (20 Å) of the molecular species detected by DOSY, which could be attributed to the monomeric forms of the **C1** conjugate. The other particles detected seem to correspond to lower diffusion coefficients (up to $1.29 \times 10^{-10} \text{ m}^2/\text{s}$) and larger sizes (up to 40 Å), which might be attributed to higher-level of aggregates (e.g. dimeric forms). DOSY provided possible evidence that **C1** molecules in aqueous may self-assemble into particles ranging in size between 20 Å and 40 Å, presumably stabilized by electrostatic interactions between the positively-charged peptide of one conjugate molecule and the negatively-charged oligonucleotide of a neighboring molecule. This self-assembly of the conjugates into supra-molecular structures might be a key factor contributing to catalysis. A number of previous studies highlighted the non-linear enhancement of the cleavage activity for this type of POCs, triggered by

concentration increase, when possible formation of catalytic multiplexes would be expected (Kovalev et al., 2008; Patutina et al., 2017, 2019; Staroseletz, Williams et al., 2017).

4. Conclusion

This research provides key information on the interactions of functional catalytically-active bioconjugates with RNA, essential for development of novel therapeutic agents with controlled chemical and biological properties, capable of recognizing and destroying disease-relevant RNAs in a highly selective manner to enhance potency and reduce potential toxicity in humans. By looking at the individual roles of the recognition and biocatalytic moieties of the conjugates toward RNA, we provide insight into the behavior of such bioconjugates against complementary and non-complementary targets and illuminate our understanding of how these bioconjugates interact with RNA sequences and catalyze their cleavage.

Very different behavior of the peptidyl and oligonucleotide components of conjugates is here revealed as selective interaction under buffered electrolyte, representative of intracellular conditions, whereas nonselective interactions arose under non-physiological conditions in water. We demonstrated here that the oligonucleotide component of the peptidyl-oligonucleotide conjugates dominate interactions between conjugates and *complementary* targets in the presence of physiological levels of counter cations (e.g. K^+), sufficient to prevent repulsion between the complementary nucleic acid strands. The important consequence of this is that in physiologically-relevant conditions, when counter cations screen the negatively-charged sugar-phosphate backbones of the RNA target, the positively-charged catalytic peptide shows poor or negligible nonspecific interactions with RNA, thus minimizing or avoiding nonspecific RNA cleavage. Indeed, the peptide component only became the key player in these interactions, when counter cations were insufficient for charge screening. This is a significant finding implying that stable nonspecific complexes between such peptidyl-oligonucleotide conjugates and RNA sequences can only be formed under non-physiological conditions, in the absence of physiological concentrations of counter cations (e.g. in de-ionized water), when nonspecific cleavage by the complexed peptide is also insignificant.

Based on these findings, it is reasonable now to assume that the '*point of contact*' between conjugates and RNA can be switched between the oligonucleotide and peptide components by simple manipulation with a few key parameters, including (i) the length and thermodynamic stability of the complementary region between the oligonucleotide recognition motif and RNA target, (ii) the availability of counter cations and (iii) the net charge of the conjugate molecules. Strong complementary binding of conjugates through the oligonucleotide recognition component may provide precise sequence-selectivity for RNA targeting, but discourage the ability of the conjugate to leave RNA after each catalytic event, thus compromising the reaction catalytic turnover. In contrast, the transient, nonspecific contacts *via* the peptide

component offer an opportunity for conjugates to '*cleave and leave*' RNA; however, this mode of binding suffers from poor target selectivity, which may ultimately lead to high systemic toxicity. Finding an appropriate balance between the sequence selectivity and sufficient level of catalytic turnover will rely on fine tuning and matching between the above parameters.

Our recent work (Patutina et al., 2017, 2019; Staroseletz, Williams et al., 2017; Williams et al., 2015) and earlier studies from other groups (Mironova et al., 2002; Mironova, Boutorine et al. 2004; Mironova, Pyshnyi, Ivanova et al., 2004; Mironova et al., 2006, 2007; Pyshnyi et al., 1997) demonstrated that the biological activity of this class of bioconjugates can only be achieved through chemical conjugation of the catalytic peptide with the oligonucleotide component. This suggested that the oligonucleotide component may induce an '*active*' conformation of the peptide to make it catalytically active by some unclear molecular interactions between the oligonucleotide and peptide components. We provide here the first direct structural evidence of the conformation necessary for sequence-selective catalysis, and the first NMR evidence of a stable, folded, hairpin-like structure of conjugates in water. Prediction and rationalization of the binding properties and hydrolytic activity of such conjugates is now strongly facilitated to allow a robust 3D structural determination of the conjugates alone and within the hybridized complexes with RNA sequences by a combination of high-resolution multi-dimensional NMR and molecular modeling. NMR spectroscopy can be used not only to illuminate the direct contacts between the different structural elements of the conjugates, but also to evaluate *inter*-nuclear distances and torsion angles, which can then serve as constraints in restrained molecular dynamic calculations using the full relaxation matrix approach. This research, which is currently in progress, will provide more detailed and clear understanding of the *structure-activity* correlations for this class of chemical ribonucleases to facilitate future rational design of the new structural variants.

Notes

1. <https://www.atdbio.com/content/1/Ultraviolet-absorbance-of-oligonucleotides>
2. <http://www.glenresearch.com/Technical/Extinctions.html>

Author contributions

EB, DC and MZ conceived and designed the experiments. Peptide and conjugate materials were synthesized by MG, SM and WZ under the supervision of EB. NMR experiments were performed by SM and WZ, and UV and fluorescent studies were carried out by MG under the direction of EB and DC. WZ undertook DOSY experiments. RNA cleavage experiments were performed by AF under the supervision of MZ. EB, DC, WZ and MZ analyzed the data and co-wrote the paper.

Acknowledgments

We are grateful to EPSRC National Mass Spectrometry Service Centre (Swansea) for providing a comprehensive mass spectrometry service. The authors would like to thank Neil O'Hara for his technical support while using optical and analytical instrumentation. We are grateful to Dr.

Harmesh Aojula for his invaluable assistance in performing peptide synthesis, especially in completing the final global deprotection and cleavage of the peptides from the resin using HF.

Disclosure statement

The authors declare that the research was conducted in the absence of any commercial or financial relationships that could be construed as a potential conflict of interest.

This work was supported by the BBSRC (grant number: BB/K012622/1), EPSRC (grant number: EP/E003400/1), EPSRC (grant number: EP/G03737X/1), as well as by the Russian Science Foundation (grant numbers: 14-44-00068 and 19-14-00250).

ORCID

Elena V. Bichenkova  <http://orcid.org/0000-0002-8186-9757>

References

- Baldini, L., Cacciapaglia, R., Casnati, A., Mandolini, L., Salvio, R., Sansone, F., & Ungaro, R. (2012). Upper rim guanidinocalix [4] arenes as artificial phosphodiesterases. *The Journal of Organic Chemistry*, 77(7), 3381–3389. doi:10.1021/jo300193y
- Beloglazova, N. G., Fabani, M. M., Zenkova, M. A., Bichenkova, E. V., Polushin, N. N., Sil'nikov, V. N., Douglas, K. T., & Vlassov, V. V. (2004). Sequence-specific artificial ribonucleases. I. Bis-imidazole-containing oligonucleotide conjugates prepared using precursor-based strategy. *Nucleic Acids Research*, 32(13), 3887–3897. doi:10.1093/nar/gkh702
- Bennett, C. F., Baker, B. F., Pham, N., Swayze, E., & Geary, R. S. (2017). Pharmacology of Antisense Drugs. *Annual Review of Pharmacology and Toxicology*, 57(1), 81–105. doi:10.1146/annurev-pharmtox-010716-104846
- Bennett, C. F., & Swayze, E. E. (2010). RNA targeting therapeutics: Molecular mechanisms of antisense oligonucleotides as a therapeutic platform. *Annual Review of Pharmacology and Toxicology*, 50(1), 259–293. doi:10.1146/annurev.pharmtox.010909.105654
- Bichenkova, E. V., Lang, Z., Yu, X., Rogert, C., & Douglas, K. T. (2011). DNA-mounted self-assembly: New approaches for genomic analysis and SNP detection. *Biochimica et Biophysica Acta (BBA) - Gene Regulatory Mechanisms*, 1809(1), 1–23. doi:10.1016/j.bbagr.2010.11.002
- Bichenkova, E. V., Raju, A. P. A., Burusco, K. K., Kinloch, I. A., Novoselov, K. S., & Clarke, D. J. (2017). NMR detects molecular interactions of graphene with aromatic and aliphatic hydrocarbons in water. *2D Materials*, 5(1), 015003. doi:10.1088/2053-1583/aa8abe
- Casi, G., & Neri, D. (2015). Antibody-drug conjugates and small molecule-drug conjugates: Opportunities and challenges for the development of selective anticancer cytotoxic agents. *Journal of Medicinal Chemistry*, 58(22), 8751–8761. doi:10.1021/acs.jmedchem.5b00457
- Chari, R. V. J. (2008). Targeted cancer therapy: Conferring specificity to cytotoxic drugs. *Accounts of Chemical Research*, 41(1), 98–107. doi:10.1021/ar700108g
- Chen, X. J., Sanchez-Gaytan, B. L., Hayik, S. E. N., Fryd, M., Wayland, B. B., & Park, S. J. (2010). Self-assembled hybrid structures of DNA block-copolymers and nanoparticles with enhanced DNA binding properties. *Small*, 6(20), 2256–2260. doi:10.1002/smll.201001185
- Crisalli, P., & Kool, E. T. (2011). Multiple pathway quenchers: Efficient quenching of common fluorophores. *Bioconjugate Chemistry*, 22(11), 2345–2354. doi:10.1021/bc200424r
- Garzon, R., Marcucci, G., & Croce, C. M. (2010). Targeting microRNAs in cancer: Rationale, strategies and challenges. *Nature Reviews Drug Discovery*, 9(10), 775–789. doi:10.1038/nrd3179
- Holoch, D., & Moazed, D. (2015). RNA-mediated epigenetic regulation of gene expression. *Nature Reviews Genetics*, 16(2), 71–84. doi:10.1038/nrg3863
- Johansson, M. K., Fidler, H., Dick, D., & Cook, R. M. (2002). Intramolecular dimers: A new strategy to fluorescence quenching in dual-labeled oligonucleotide probes. *Journal of the American Chemical Society*, 124(24), 6950–6956. doi:10.1021/ja025678o
- Kersebaum, R., & Salnikov, G. (2006). *DOSY and diffusion by NMR* (pp. 1–32). Bruker BioSpin GmbH.
- Kole, R., Krainer, A. R., & Altman, S. (2012). RNA therapeutics: Beyond RNA interference and antisense oligonucleotides. *Nature Reviews Drug Discovery*, 11(2), 125–140. doi:10.1038/nrd3625
- Kovalev, N. A., Medvedeva, D. A., Zenkova, M. A., & Vlassov, V. V. (2008). Cleavage of RNA by an amphiphilic compound lacking traditional catalytic groups. *Bioorganic Chemistry*, 36(2), 33–45. doi:10.1016/j.bioorg.2007.10.003
- Krishna, M. S., Wang, Z., Zheng, L., Bowry, J., Ong, A. A. L., Mu, Y., Prabakaran, M., & Chen, G. (2019). Incorporating G-C pair-recognizing guanidinium into PNAs for sequence and structure specific recognition of dsRNAs over dsDNAs and ssRNAs. *Biochemistry*, 58(36), 3777–3788. doi:10.1021/acs.biochem.9b00608
- Lonnberg, H. (2011). Cleavage of RNA phosphodiester bonds by small molecular entities: A mechanistic insight. *Organic & Biomolecular Chemistry*, 9, 1687–1703. doi:10.1039/C0OB00486C
- Marras, S. A. E., Kramer, F. R., & Tyagi, S. (2002). Efficiencies of fluorescence resonance energy transfer and contact-mediated quenching in oligonucleotide probes. *Nucleic Acids Research*, 30, e122. doi:10.1093/nar/gnf121
- Marras, S. A. E., Tyagi, S., & Kramer, F. R. (2006). Real-time assays with molecular beacons and other fluorescent nucleic acid hybridization probes. *Clinica Chimica Acta*, 363(1-2), 48–60. doi:10.1016/j.cccn.2005.04.037
- Milligan, J. F., & Uhlenbeck, O. C. (1989). Synthesis of small RNAs using T7 RNA polymerase. *Methods in Enzymology*, 180, 51–62. doi:10.1016/0076-6879(89)80091-6
- Mironova, N. L., Boutorine, Y. I., Pyshnyi, D. V., Ivanova, E. M., Zenkova, M. A., & Vlassov, V. V. (2004). Ribonuclease activity of the peptides with alternating arginine and leucine residues conjugated to tetrathymidilate. *Nucleosides, Nucleotides and Nucleic Acids*, 23(6-7), 885–890. doi:10.1081/NCN-200026036
- Mironova, N. L., Pyshnyi, D. V., & Ivanova, E. M. (2004). RNA-cleaving oligonucleotide-peptide conjugates. In M. A. Zenkova (Ed.), *Artificial nucleases. Nucleic acids and molecular biology* (Vol. 13, p. 151–172). Springer.
- Mironova, N. L., Pyshnyi, D. V., Ivanova, E. M., Zarytova, V. F., Zenkova, M. A., Gross, H. J., & Vlassov, V. V. (2002). Sequence-specific cleavage of the target RNA with oligonucleotide-peptide conjugates. *Russian Chemical Bulletin*, 51(7), 1177–1186. doi:10.1023/A:1020932009136
- Mironova, N. L., Pyshnyi, D. V., Ivanova, E. M., Zenkova, M. A., Gross, H. J., & Vlassov, V. V. (2004). Covalently attached oligodeoxyribonucleotides induce RNase activity of a short peptide and modulate its base specificity. *Nucleic Acids Research*, 32(6), 1928–1936. doi:10.1093/nar/gkh514
- Mironova, N. L., Pyshnyi, D. V., Stadler, D. V., Prokudin, I. V., Boutorine, Y. I., Ivanova, E. M., Zenkova, M. A., Gross, H. J., & Vlassov, V. V. (2006). G-specific RNA-cleaving conjugates of short peptides and oligodeoxyribonucleotides. *Journal of Biomolecular Structure and Dynamics*, 23(6), 591–602. doi:10.1080/07391102.2006.10507084
- Mironova, N. L., Pyshnyi, D. V., Shtadler, D. V., Fedorova, A. A., Vlassov, V. V., & Zenkova, M. A. (2007). RNase T1 mimicking artificial ribonuclease. *Nucleic Acids Research*, 35(7), 2356–2367. doi:10.1093/nar/gkm143
- Niittymaki, T., & Lonnberg, H. (2006). Artificial ribonucleases. *Organic & Biomolecular Chemistry*, 4, 15–25. doi:10.1039/B509022A
- Olejko, L., & Bald, I. (2017). FRET efficiency and antenna effect in multi-color DNA origami-based light harvesting systems. *RSC Advances*, 7(39), 23924–23934. doi:10.1039/C7RA02114C
- Olejko, L., Cywiński, P. J., & Bald, I. (2016). An ion-controlled four-color fluorescent telomeric switch on DNA origami structures. *Nanoscale*, 8(19), 10339–10347. doi:10.1039/C6NR00119J
- Patutina, O. A., Bichenkova, E. V., Miroshnichenko, S. K., Mironova, N. L., Trivoluzzi, L. T., Burusco, K. K., Bryce, R. A., Vlassov, V. V., & Zenkova, M. A. (2017). miRNases: Novel peptide-oligonucleotide bioconjugates

- that silence miR-21 in lymphosarcoma cells. *Biomaterials*, 122, 163–178. doi:10.1016/j.biomaterials.2017.01.018
- Patutina, O. A., Miroshnichenko, S. K., Mironova, N. L., Sen'kova, A. V., Bichenkova, E. V., Clarke, D. J., Vlassov, V. V., & Zenkova, M. A. (2019). Catalytic knockdown of miR-21 by artificial ribonuclease: Biological performance in tumor model. *Frontiers in Pharmacology*, 10, 879. doi:10.3389/fphar.2019.00879
- Provencher, S. W. (1982a). CONTIN: A general purpose constrained regularization program for inverting noisy linear algebraic and integral equations. *Computer Physics Communications*, 27(3), 229–242. doi:10.1016/0010-4655(82)90174-6
- Provencher, S. W. (1982b). A constrained regularization method for inverting data represented by linear algebraic or integral equations. *Computer Physics Communications*, 27(3), 213–227. doi:10.1016/0010-4655(82)90173-4
- Pyshnyi, D., Repkova, D. M., Lokhov, S., Ivanova, E., Venyaminova, A., & Zarytova, V. (1997). Oligonucleotide-peptide conjugates for RNA cleavage. *Nucleosides and Nucleotides*, 16(7-9), 1571–1574. doi:10.1080/07328319708006232
- Romero-Barrios, N., Legascue, M. F., Benhamed, M., Ariel, F., & Crespi, M. (2018). Splicing regulation by long noncoding RNAs. *Nucleic Acids Research*, 46(5), 2169–2184. doi:10.1093/nar/gky095
- Scannell, J. W., Blanckley, A., Boldon, H., & Warrington, B. (2012). Diagnosing the decline in pharmaceutical R&D efficiency. *Nature Reviews Drug Discovery*, 11(3), 191–200. doi:10.1038/nrd3681
- Silberklang, M., Gillum, A. M., & RajBhandary, U. L. (1979). Use of in vitro ³²P-labeling in the sequence analysis of nonradioactive tRNAs. *Methods in Enzymology*, 59, 58–109. doi:10.1016/0076-6879(79)59072-7
- Salvio, R., & Casnati, A. (2017). Guanidinium promoted cleavage of phosphoric diesters: Kinetic investigations and calculations provide indications on the operating mechanism. *The Journal of Organic Chemistry*, 82(19), 10461–10469. doi:10.1021/acs.joc.7b01925
- Salvio, R., Mandolini, L., & Savelli, C. (2013). Guanidine–guanidinium cooperation in bifunctional artificial phosphodiesterases based on diphenylmethane spacers; gem-dialkyl effect on catalytic efficiency. *The Journal of Organic Chemistry*, 78(14), 7259–7263. doi:10.1021/jo401085z
- Staroseletz, Y., Nechaev, S., Bichenkova, E., Bryce, R., Watson, C., Vlassov, V., & Zenkova, M. (2017). Non-enzymatic recombination of RNA: Ligation in loops. *Biochimica et Biophysica Acta (BBA) - General Subjects*, 1862(3), 705–725. doi:10.1016/j.bbagen.2017.10.019
- Staroseletz, Y., Williams, A., Burusco, K. K., Alibay, I., Vlassov, V. V., Zenkova, M. A., & Bichenkova, E. V. (2017). Dual' peptidyl-oligonucleotide conjugates: Role of conformational flexibility in catalytic cleavage of RNA. *Biomaterials*, 112, 44–61. doi:10.1016/j.biomaterials.2016.09.033
- Stewart, J. M., & Young, J. D. (1979). *Solid phase peptide synthesis* (pp. 105–107). Pierce Chemical Co.
- Tsourkas, A., Behlke, M. A., Xu, Y., & Bao, G. (2003). Spectroscopic features of dual fluorescence/luminescence resonance energy-transfer molecular beacons. *Analytical Chemistry*, 75(15), 3697–3703. doi:10.1021/ac034295I
- Valentini, M., Vaccaro, A., Rehor, A., Napoli, A., Hubbell, J. A., & Tirelli, N. (2004). Diffusion NMR spectroscopy for the characterization of the size and interactions of colloidal matter: The case of vesicles and nanoparticles. *Journal of the American Chemical Society*, 126(7), 2142–2147. doi:10.1021/ja037247r
- Williams, A., Staroseletz, Y., Zenkova, M., Jeannin, L., Aojula, H., & Bichenkova, E. (2015). Peptidyl-oligonucleotide conjugates demonstrate efficient cleavage of RNA in a sequence-specific manner. *Bioconjugate Chemistry*, 26(6), 1129–1143. doi:10.1021/acs.bioconjchem.5b00193
- Zhang, X., Ma, X., Jing, S., Zhang, H., & Zhang, Y. (2018). Non-coding RNAs and retroviruses. *Retrovirology*, 15(1), 20. doi:10.1186/s12977-018-0403-8
- Zhao, C., Hellman, L. M., Zhan, X., Bowman, W. S., Whiteheart, S. W., & Fried, M. G. (2010). Hexahistidine-tag-specific optical probes for analyses of proteins and their interactions. *Analytical Biochemistry*, 399(2), 237–245. doi:10.1016/j.ab.2009.12.028